



Article

Application of SIM, HSPIV, BTM, and BIV Techniques for Evaluations of a Two-Phase Air–Water Chute Aerator Flow

James Yang ^{1,2} , Chang Lin ^{3,*}, Ming-Jer Kao ³, Penghua Teng ¹  and Rajkumar V. Raikar ⁴

¹ Division of Resources, Energy and Infrastructure, Royal Institute of Technology (KTH), 10044 Stockholm, Sweden; jamesya@kth.se (J.Y.); teng.penghua@byv.kth.se (P.T.)

² Vattenfall AB, R&D Hydraulic Laboratory, 81426 Älvkarleby, Sweden

³ Department of Civil Engineering, National Chung Hsing University, Taichung 40227, Taiwan; mjkao1976@gmail.com

⁴ Department of Civil Engineering, KLE Dr. M. S. Sheshgiri College of Engineering and Technology, Belgaum 590008, India; rvraikar@gmail.com

* Correspondence: chenglin@nchu.edu.tw; Tel.: +886-4-2285-5182

Received: 2 September 2018; Accepted: 2 November 2018; Published: 6 November 2018



Abstract: Four image-based techniques—i.e., shadowgraphic image method (SIM), high-speed particle image velocimetry (HSPIV), bubble tracking method (BTM), and bubble image velocimetry (BIV)—are employed to investigate an aerator flow on a chute with a 17° inclination angle. The study focuses on their applications to the following issues: (1) to explore the characteristic positions of three water–air interfaces; (2) to interpret the evolution process of air bubbles shed from the wedged tip of the air cavity; (3) to identify the probabilistic means for characteristic positions near the fluctuating free surface; (4) to explore the probability distribution of intermittent appearance of air bubbles in the flow; (5) to obtain the mean streamwise and transverse velocity distributions of the water stream; (6) to acquire velocity fields, both instantaneous and mean, of air bubbles; (7) to construct a two-phase mean velocity field of both water flow and air-bubbles; and (8) to correlate the relationship among the probability distribution of air bubbles, the mean streamwise and transverse velocity profiles of air bubbles, and water stream. The combination of these techniques contributes to a better understanding of two-phase flow characteristics of the chute aerator.

Keywords: aerator; two-phase flow; air cavity; shadowgraphic image method (SIM); high-speed particle image velocimetry (HSPIV); bubble tracking method (BTM); bubble image velocimetry (BIV); flow impingement point; air bubbles

1. Introduction

1.1. Survey of Related Chute Flow

In recent decades, cavitation damage in concrete surfaces of many spillways and chutes has been reported at e.g., Keban Dam in Turkey and Karum Dam in Iran [1,2]. Nowadays, spillway aerators are commonly used in spillways subjected to high velocity to counteract erosion damages due to cavitation. Three types of aerators are common, i.e., transverse offset, deflector, and their hybrids. The aerator lifts the approach flow from the boundary to build up an air cavity and a free jet with an upper and a lower surface—air is entrained into the water flow from both surfaces. A two-phase flow of water–air mixture is generated and propagates downstream, thus protecting the chute bottom from cavitation damages. Air to the aerator is usually supplied via air shafts connected to the atmosphere.

Pan et al. [3] and Pinto et al. [4] were among the first to put forward a method to calculate the air entrainment coefficient, i.e., the ratio of air-flow rate of the aerator to water-flow rate of the spillway. A linear equation for the coefficient was also developed by incorporating the length of the free jet. Pinto and Neidert [5] showed later that, for a given geometric layout of an aerator, the air entrainment coefficient was mainly a function of the Froude number, the Euler number, and the ratio of deflector height to the approach flow depth.

Presented at the IAHR Symposium on Scale Effects in Esslingen, Germany, 1984, a few papers dealt with chute aerators. Wood [6] addressed the differences in air entrainment between from the upper free surface and from the air cavity. Volkart and Rutschmann [7] discussed the model-prototype conformity based on model scales from 1:1 to 1:18.75, in which strong scale effects were evident for the jet trajectory; a smaller aerator model led to a shorter jet. Marcano and Castillejo [8] showcased that air was entrained not only from the aerator cavity but also from the jet's upper surface. In terms of a Reynolds number limit, Pan and Shao [9] proposed criteria with regard to the choice of a model scale. If the number was larger than 3.5×10^6 , the scale effects arising from both viscous and surface tension forces could be disregarded.

Falvey and Ervine [10] examined the air entrainment in free water jets, unveiling that boundary roughness affected, in fully turbulent flows, the air entrainment coefficient. Rutschmann [11] stated that the air entrainment phenomenon was shear-dominated; the entrained amount of air depended linearly on the relative jet length. After testing several aerator geometries, Wood [12] pointed out that air entrainment was ascribable to spray and nappe entrainment with different features in the approach flow, cavity zone, impact zone, and downstream flow.

Rutschmann and Hager [13] adopted two approaches that related the air entrainment coefficient to parameters of chute slope, deflector angle, deflector/offset height, approach flow depth, and velocity and air cavity sub-pressure. With a series of laboratory tests, Gaskin et al. [14] expressed the air entrainment coefficient in terms of chute slope, deflector angle, and a Froude number of the approach flow. The air entrainment coefficient and air concentration downstream were based on two formulas resulting from the experimental data. Kramer et al. [15], Kramer and Hager [16], and Kramer et al. [17] presented experimental air concentration profiles downstream of a chute aerator, emphasizing the streamwise air detrainment in the far field.

In model tests, Jalili Ghazizadeh et al. [18] showcased vertical air concentration distributions along the lower jet surface and proposed an empirical equation for concentration prediction. In relation to flow and geometric parameters, Pfister and Hager [1,2] illustrated experimental air concentration distributions in the near and far fields, with the purpose of predicting the development of streamwise air concentration. The aerator flow was usually classified into jet zone, reattachment and spray zone, and far-field zone. The key parameters that governed the air transport downstream of an aerator included approach-flow Froude number, chute slope, and deflector angle [19].

1.2. Survey of Measurement Items and Techniques for Other Two-Phase Flows

Hydraulic jumps involve also a two-phase phenomenon. Using the hot-film anemometry, Resch et al. [20] studied distributions of air concentration and air-bubble dimensions in a hydraulic jump. Mossa and Tolve [21] visualized the jump flow structure and determined the location of the maximum air concentration. With dual-tip conductivity probes, Chanson and Brattberg [22] examined the air–water flow features in a hydraulic jump's shear region, indicating that the air concentration distribution follows the solution of the diffusion equation; the velocity profile follows a similar shape to a wall jet's. With an optical probe, Murzyn et al. [23] examined the air-bubble characteristics in a hydraulic jump and they showed that in its lower part, the air concentration profile accorded with the Gaussian distribution; in its upper part the profile was approximated with the error function.

In past decades, non-intrusive optics-based methods, inclusive of particle image velocimetry (PIV), have found their use in research of two-phase flow fields. Hornung et al. [24] was among the first to use the PIV technique for measurements of flow velocity fields in a hydraulic jump. In addition

to velocity measurements, Lennon and Hill [25] also visualized the flow structure of a weak hydraulic jump with little air entrainment (the Froude number = 1.4–3.0). It was noted that the entrained air bubbles resulted in strong scattering of laser light, which severely influenced the accuracy of the measurements in the roller region with high air content. Recently, Misra et al. [26] presented the velocity pattern of a weak hydraulic jump, with emphasis laid on turbulence generation in spilling breakers and in the surf zone. Lately, Bercovitz et al. [27] employed a large-scale PIV to explore the surface velocity field of a plunging water jet from a sharp-crested weir. The main targets of their study focused on the Nappe trajectory and characteristic length, along which the energy dissipation becomes prominent.

These studies contributed in one way or another to the understanding of air–water flow fields, especially air concentration features in hydraulic jumps. Nevertheless, the measurements with the non-intrusive technique in hydraulic jumps were either outside the aerated region or limited to the submerged and weak jumps in which little air was entrained. This was mainly due to technique limitations.

With a fiber optic reflectometer, Chang et al. [28] presented the experimental results of velocity and void fraction ratio in air–water flows, including free jets and bubbling water columns. Ryu et al. [29] developed a new non-intrusive methodology, i.e., the bubble image velocimetry (BIV). By correlating the texture of air–water interfaces in images, it incorporated the PIV method into the shadowgraphic image method (SIM) for velocity measurements in the mixture. In an offshore model, Ryu et al. [30] demonstrated the technique in measurements of overtopping green water due to breaking wave impingement. Combining the tracking technique with the SIM, Kashima et al. [31], Mori et al. [32], and Mori and Kakuno [33] investigated air bubble sizes and void fraction ratio of regular breaking waves during an air entrainment process. Pairing the BIV with the high-speed PIV technique (HSPIV, >1000 frames/s), Lin et al. [34] obtained, in a periodic oscillatory flow at a drop structure, its velocity fields of the aerated region. Lin et al. [35] elucidated the self-similarity of velocity fields in steady-state hydraulic jumps, in which the Froude number of the approach flow was in the range of 4.51–5.32.

Karn et al. [36] developed an integrative measurement technique coupled with image-processing algorithms to explore bubbly flows where the bubble size distribution featured a wide range. They found that its obstacles were large air-bubble clusters, high unsteadiness, high air content, and air-bubble overlapping in the images. Furthermore, from the visualized pictures of air bubbles (illuminated with a 500 W halogen lamp and captured with a high-resolution camera) and visual identification, Besagni and Inzoli [37] investigated, for air bubbles moving upwards through an annular gap bubble column within a cylindrical tank with two pipes, their size distributions, shapes, and aspect ratios.

Lin et al. [38] employed the function *imadjust* (IA) with histogram specification [39,40] to further realize the contrast enhancement of HSPIV images. From gray-level gradients in the smoothed ‘brightness’ distribution of the contrast-enhanced seeding particles, they determined the probabilistic mean features of a spillway aerator flow. However, its application to explore the flow field within a sliding jet encountered both difficulties and challenges. This was mainly due to the fact that air bubbles shed successively from the air cavity, propagating then into the sliding jet. Once the flow field was illuminated by laser light sheet in the HSPIV measurements, air bubbles reflected the strong scattering light. This made it impossible to measure the air-bubble velocity or identify air-bubble contours.

1.3. Key Issues Unknown or Rudimentary

Based on the literature survey, the previous studies on two-phase chute flows have, in relation to governing flow and geometric parameters, focused on air entrainment rate, air cavity sub-pressure, air concentration, and air-bubble sizes. Despite this, the most fundamental knowledges are to date still limited or rudimentary and this concerns the following issues. (1) Where are the locations of the interface between the upper surface of the free (or sliding) jet and the atmosphere? (2) Where are the positions of the interface between the upper/lower boundary of air cavity and the lower jet

surface/the surface of the recirculation flow? (3) How is the discrete air-bubbles generated from the wedged tip of air cavity with what kinds of evolution process? (4) What is the probability distribution of air-bubbles downstream the wedged tip of air cavity? (5) How to determine the instantaneous streamwise and transverse velocities of an air bubble? (6) How to determine the air-bubble velocity field? (7) What are the features of instantaneous and mean velocity fields of both water stream and air bubbles? Finally, (8) What are the relationships among the probability distribution of air bubbles, the mean streamwise/transverse velocity profiles of air bubbles, and the counterparts of water stream?

For measuring water–air interfaces, air-bubble contours and corresponding velocity fields of air bubbles, utilization of appropriate techniques, which are other than those used by Lin et al. [38] for HSPIV measurements of free jets, becomes necessary. The present study therefore lays emphasis on applications of SIM, HSPIV, BTM, and BIV to explore the two-phase-related issues mentioned above.

In the section that follows, the experimental set-up and instrumentation are introduced. The results and discussions are presented in Section 3. Conclusions and remarks are given in Section 4.

2. Experimental Set-Up and Procedure

2.1. Water Flume and Aerator Model

Laboratory experiments are carried out in a recirculating flume at National Chung Hsing University, Taiwan. The test section is 3.05 m long, 0.50 m wide, and 0.54 m high, placed 3.0 m from the flume inlet and surrounded by glass walls and glass bottom to facilitate optical access. A rectangular honeycomb, consisting of a bundle of straws (1.0 cm in diameter and 9.0 cm in length) is installed at the chute inlet to eliminate the eddy-like structure potentially generated due to use of a vertical plate (Figure 1a) and to smoothen the incoming flow, thus achieving a uniform approach flow.

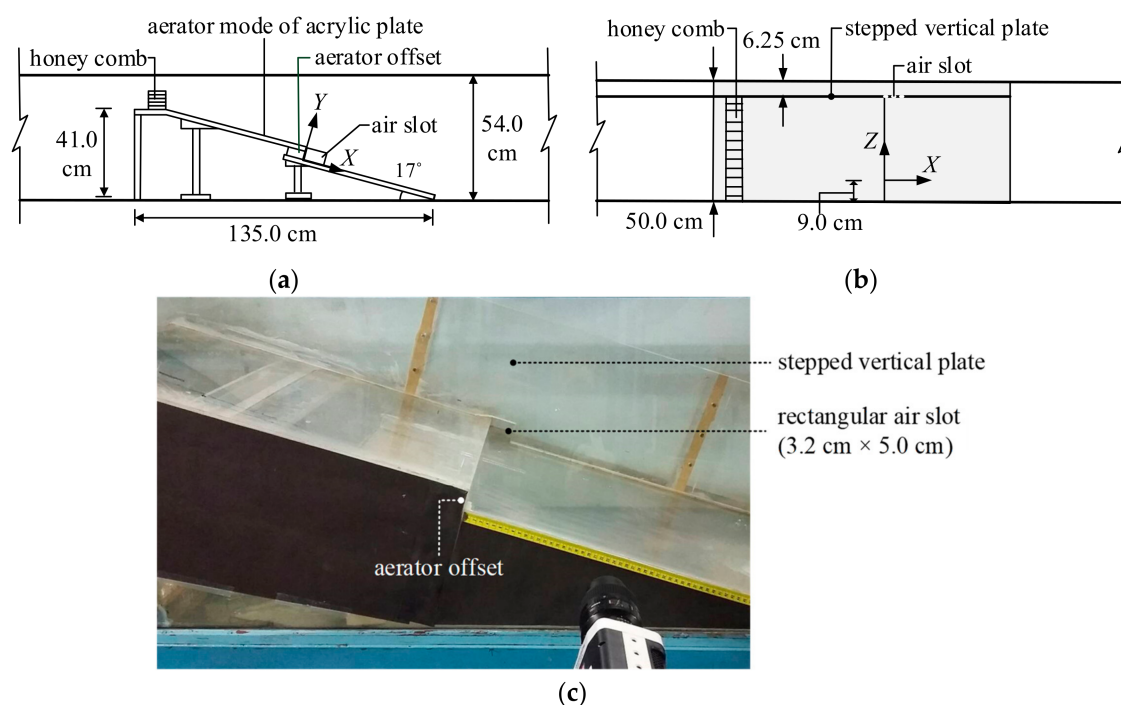


Figure 1. Schematic diagram of the aerator model mounted in the test section: (a) side view; (b) top view; (c) photo showing deployment of the offset, stepped vertical plate, and air slot.

Figure 1a,b shows schematically the aerator model of acrylic plate. The model has a horizontal length of 135.0 cm, a spanwise width of 49.5 cm, and a vertical height of 41.0 cm; the aerator offset height is $H = 3.2$ cm. For enhancing understanding of the deployment, Figure 1c illustrates a snapshot of the chute surface, together with the offset and a rectangular air slot. The chute inclination angle is

17°. The aerator is composed of only an offset, without any deflector and groove. A stepped vertical plate (120.0 cm long), extending from upstream of the honeycomb to farther downstream of the offset, is mounted flush over the stepped-chute part and parallel to the rear glass side-wall with a clear spacing of 6.25 cm between them. Natural ventilation through a rectangular air slot (3.2×5.0 cm in size), placed immediately downstream of the offset and on the intersecting zone of the stepped vertical plate and the stepped-chute part (Figure 1a), is provided for air supply. Under such a situation, sufficient amount of air is conveyed into the air cavity, in which the atmospheric pressure is sustained. Note that use of a too small size of the air slot (say 1.0×1.5 cm) would cause insufficient air supply, thus resulting in the air cavity pressure lower than the atmospheric pressure and unexpected oscillation of the free jet.

A cartesian coordinate system (X, Y, Z) is used, with origin at the offset bottom and 9.0 cm away from the front glass wall (see Figure 1a,b); their positive directions point downstream, upwards, and towards the rear glass wall, respectively.

2.2. HSPIV Measurement of Velocity Field and Profiles of Water Stream

The HSPIV system is used to measure the 2D velocity field of water stream in the (free or sliding) jet and non-aerated zone of the two-phase flow. This system comprises a high-speed digital camera, light source, cylindrical lens and advanced software for image processing. The light source is a 5 W argon-ion laser head (Coherent I-90), from which a laser beam is emitted and guided through a cylindrical lens, thus forming a light sheet with a thickness of 1.5 mm. The light sheet is eventually projected from the top of the flume down into the flow (Figure 2a) at 9.0 cm behind the inner side of front glass wall. This allocation aims to minimize the overlapping and blockage effect of the water-air interfaces and air-bubbles (generated between the front glass wall and the laser light sheet) on the quality of images, and to avoid the boundary effect induced by the glass wall (Li [41]). Aluminum particles with a 10 μm mean diameter and a 2.7 specific gravity are used as tracers. The particle settling velocity (by Stoke's law) is less than 0.01 cm/s, much lower than the velocity of interest in the study. These particles were seeded into water flow upstream of the honeycomb.

To capture the particle laden images, a high-speed digital camera (Vision Research, Phantom M310), with a maximum pixel resolution of 1280×800 and a maximum framing rate of 3200 Hz, is used. To allow a high image resolution and appropriate magnification of the measured area, a Nikon 105 mm lens ($f/2.8\text{D}$ AF Micro-Nikkor) is fitted to the camera. Two fields of view for HSPIV measurements (FOVP_1 and FOVP_2) are considered for obtaining detailed velocity field of water stream. Their size is 5.22×4.08 cm, equivalent to a conversion factor of 196.1 pixel/cm or 0.0051 cm/pixel. These two fields of view cover the streamwise distance from $X = 10.8$ to 18.0 cm with an overlapping of 3.2 cm. To ensure a high time-resolved HSPIV algorithm, a 4000 Hz camera framing rate with a pixel resolution of 1024×800 is set to capture the images with a 2.25 s sampling duration (i.e., a total of 9000 samples) for each run. Three repeated tests are run for each field of view. The captured images are then processed using cross-correlation technique (MPIV Fortran edition, Mori and Chang [42] and Adrian [43]) to acquire the instantaneous velocity field of water stream. A multi-grid interrogation procedure, starting at 64×64 pixels and ending at 8×8 pixels with 50% overlap, is applied in processing the data. Note that the velocity data at all pixel points in the overlapping area are the means of the corresponding velocities obtained in both FOVP_1 and FOVP_2 .

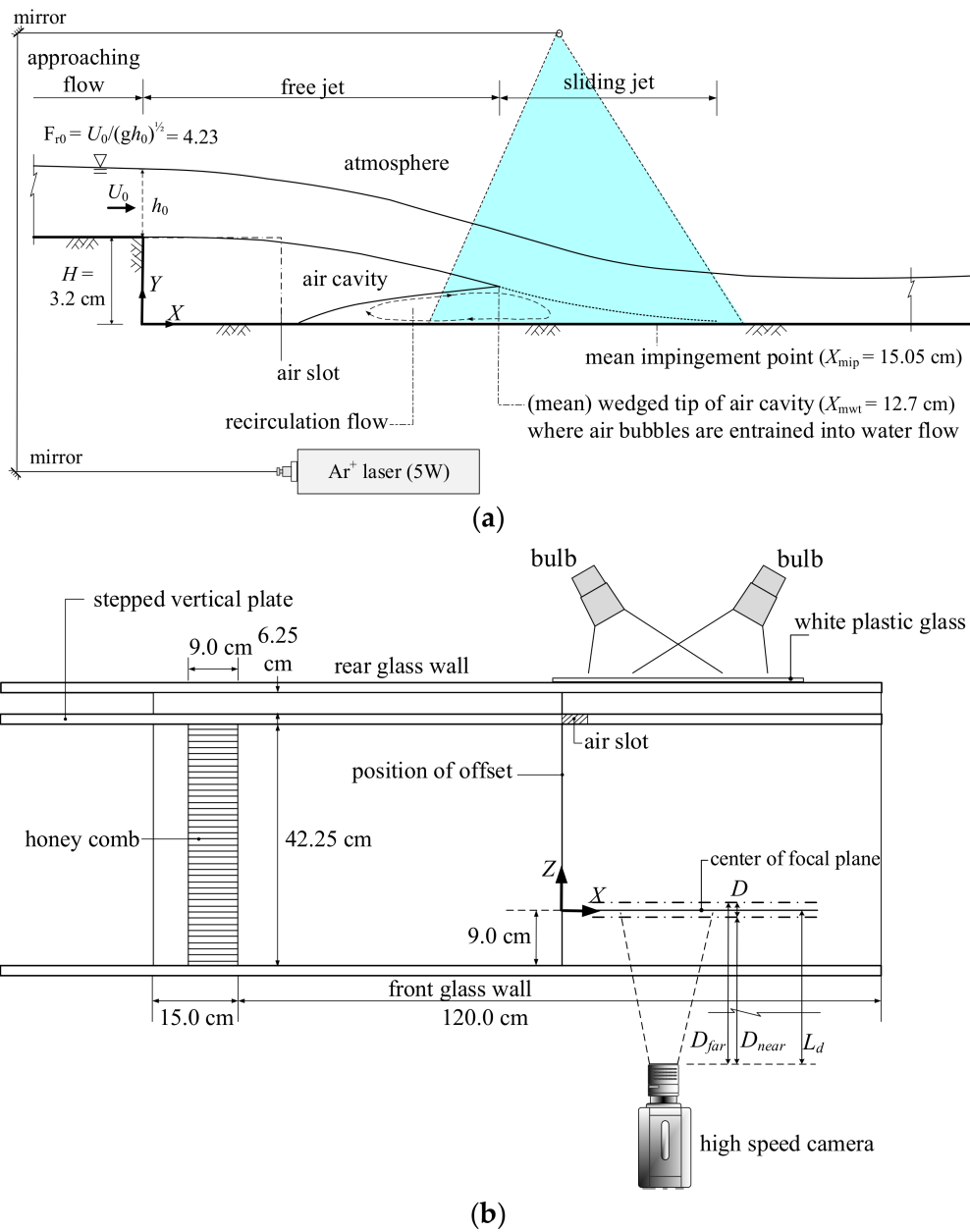


Figure 2. Schematic diagram showing (a) illumination of flow field using laser light sheet for HSPIV measurement; (b) deployment of the depth of field (with thickness D) and two bulbs for SIM observation and BIV analysis.

2.3. SIM for Identifying Water–Air Interface and BTM for Measuring Velocities of Individual Air Bubbles

It is known that gray-level differences in the images are easily formed at arbitrary water–air interfaces and around air-bubble contours while illuminated by bulb flood-light. Such kind of gray-level difference on the interface thus introduces easily the so-called ‘shadow’ in the image processing. Using this shadow feature, determination of water–air interface, identification of the position for air-bubble contour, and measurement of air-bubble velocity are realized.

Figure 2b shows the SIM setup with two 600 W light bulbs mounted behind the rear glass wall for illumination. A thin translucent plastic sheet is specially attached to the rear glass wall to create uniform illumination on the flow and to enhance the shadows of the water–air interfaces or air-bubble contours in the images. The center of focal plane is located at a distance of 9.0 cm behind the inner side of the front glass wall. This separation can play an important role in minimizing the blockage and

overlapping effect of the water–air interfaces and air bubbles on the image quality and in avoiding the boundary effect caused by the glass wall (Li [41]). The camera is particularly fitted with a lens of 105-mm focal length, which has very sharp discrimination capacity. The use of this lens allows the water–air interfaces and air-bubble contours only within the depth of field (DOF, acting as a virtual light sheet) to be recorded clearly in the images.

The thickness of the DOF, D , is estimated by (Ryu et al. [29])

$$D = D_{\text{far}} - D_{\text{near}} \quad (1)$$

in which D_{far} and D_{near} denoting the farthest and nearest distances between the camera lens and the DOF are expressed as

$$D_{\text{far}} = L_d f_d^2 / (f_d^2 - N_a L_d C) \quad (2)$$

$$D_{\text{near}} = L_d f_d^2 / (f_d^2 + N_a L_d C) \quad (3)$$

where L_d denotes the distance between the lens and the central focal plane within the DOF, f_d is the focal distance of the camera lens, C represents a constant for the circle of confusion, and N_a is the aperture value of the camera lens. The measuring error due to finite thickness of the DOF (Ryu et al. [29]) is estimated by

$$E_{\text{error}} = D/2L_d \quad (4)$$

To achieve optimal deployment and high precision for the SIM measurements, the parameters are set as: $L_d = 765.0$ mm, $f_d = 60.0$ mm, $C = 0.03$ mm, and $N_a = 2.8$, leading to $D_{\text{far}} = 778.9$ mm, $D_{\text{near}} = 751.6$ mm, $D = 27.3$ mm, and $E_{\text{error}} = 1.78\%$. The value of E_{error} is so small that the effect of the DOF is neglected.

The high-speed digital camera used for the SIM tests is the same as that for the HSPIV measurements. In the former, the upper and lower edges of the camera view field are also adjusted exactly parallel to the surface of the stepped-chute part. To obtain a global view for the two-phase flow, the first field of view in the SIM runs (FOVS₁) for -0.2 cm $\leq X \leq 30.5$ cm is considered with a relatively large size of 30.7 cm long \times 12.0 cm high. In addition, to acquire finer images with clear water–air interfaces and air-bubble contours for 10.8 cm $\leq X \leq 18.1$ cm, the second field of view for the SIM (FOVS₂) is taken into account. The size of FOVS₂ is 7.30 cm long \times 5.70 cm high, equal to a conversion factor of 140.3 pixel/cm or 0.00713 cm/pixel. No laser light sheet is needed in the SIM experiments. For each run of FOVS₁/FOVS₂ in the SIM test, the camera operates at a framing rate of 1000/3000 Hz under a resolution of (1024 \times 400)/(1024 \times 800) pixel. For reference use, only one run is done for FOVS₁ with 4000 images. However, three repeated runs with a total of 27,000 images are carried out for FOVS₂.

The BTM is also employed to trace the movements of air bubbles within the ‘water column’ in the SIM images for 16.5 cm $\leq X \leq 17.5$ cm (details given in Section 3.5.). Accordingly, the instantaneous streamwise/transverse velocities of air bubbles targeted can be determined, aiming to further acquire the depth-averaged streamwise/transverse velocity profile of air bubbles at $X = 17.0$ cm. These two velocity profiles are used to validate the mean results obtained in the BIV analysis.

2.4. BIV Analysis for Velocity Profiles and Field of Air Bubbles

The BIV technique developed by Ryu et al. [29]) is used for obtaining the velocity fields and profiles of air bubbles in the aerated region. Note that BIV works only in the region where HSPIV does not run well or does not operate at all. The details of measuring principle and validated experiments of BIV measurements can be referred to Ryu et al. [29] and Lin et al. [34,35] for its application to measure the velocity fields and profiles of air bubbles in various two-phase flows, such as flow fields of the green water with high waves impinging upon a vertical wall, the entrained air bubbles in the periodical oscillatory dropping flow downstream of a vertical drop structure, and the steady hydraulic jumps with very dense air bubbles over the horizontal bottom, respectively.

The images captured in the FOVS₂ for the SIM experiments (with a 3000 Hz framing rate) are also employed to obtain the instantaneous and mean velocity fields of air bubbles by the BIV analysis. However, these velocities are, in fact, determined from the displacements of the ‘shadows of air-bubble textures’ within a time interval of 1/3000 s by using the cross-correlation technique [42,43]. A similar multi-grid interrogation process as that in the HSPIV measurements, starting at 64 × 64 pixels and ending at 8 × 8 pixels with 50% overlap between two neighboring sub-windows, is used in the process.

Error in the BIV analysis mainly consists of two sources (Ryu et al. [29]; Lin et al. [34,35]): one is the installation-related error due to a limited DOF and the other is the pixel-resolution related error in BIV image processing for the displacement determination. As stated in the SIM measurements, the first error due to the limited DOF in the measurements is about 1.78%. The second error emanating from the displacement determination can be estimated as follows. As shown later in Figure 24a, the most prominent velocity gradient in the velocity field of *air bubbles* is about 325.6 1/s [= (102.97 – 5.29) cm/s/(1.70 – 1.40) cm]. For a 3000 Hz framing rate in the BIV analysis, the gradient (in terms of displacement in pixel) is equal to 0.109 pixel/pixel [= (325.6 1/s)/(3000 1/s)] so the corresponding uncertainty is about 0.17 pixel (Keane and Adrian [44]), which is equivalent to 1.7% [= (0.17 pixel × 0.0071 cm/pixel × 3000 1/s)/(214.45 cm/s)] of $U_0 = 214.45$ cm/s at $X = 0$. Accordingly, the total relative error at the largest velocity gradient in the air-bubble velocities is 3.48%, demonstrating satisfactory results achieved in the BIV analysis.

For easy comprehension, the systematic frame structure for different roles played and distinct targets aimed by HSPIV, SIM, BTM, and BIV for the present two-phase chute flow is summarized in Figure 3.

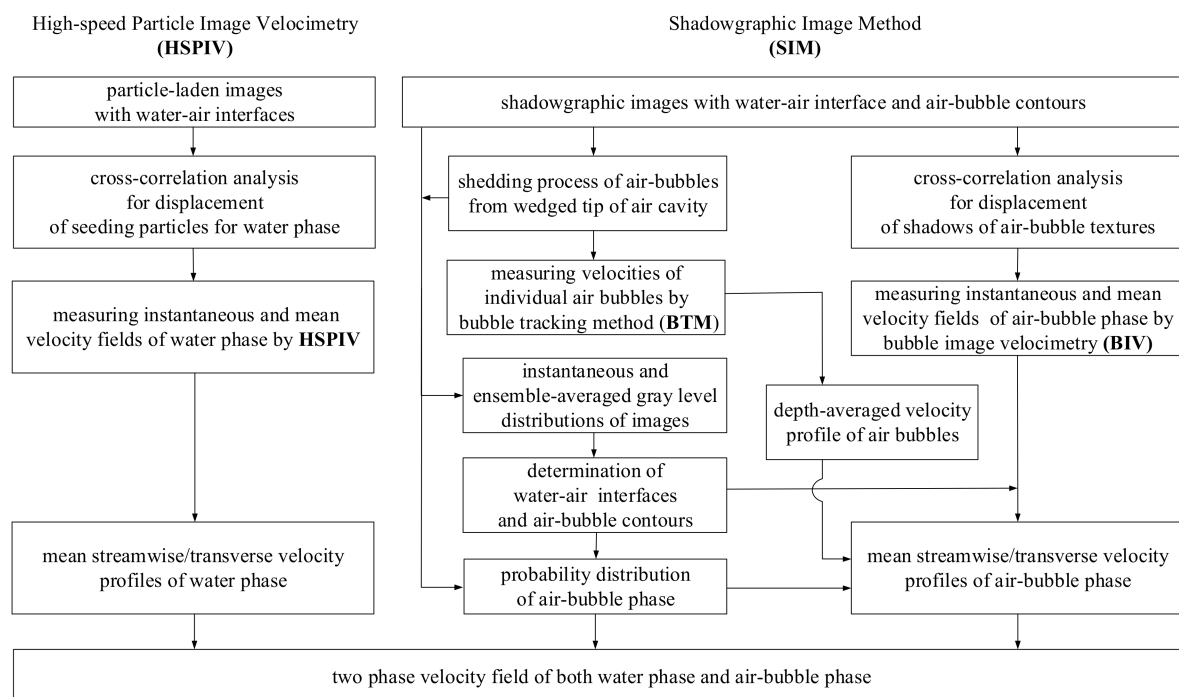


Figure 3. A systematic frame structure outlined for different roles played and distinct targets aimed by HSPIV, SIM, BTM, and BIV.

2.5. Experimental Conditions

Only one target experiment is carried out in the study. The supercritical approach-flow at $X = -4.0$ and 0 cm has the mean water depths $h_0 = 2.76$ and 2.62 cm as well as the depth-averaged velocity $U_0 = 203.84$ and 214.45 cm/s, thus resulting in the unit discharge $q_0 [=U_0 \times h_0] = 562.6$ and 561.9 cm²/s as well as the approach-flow Froude number $F_{r0} [=U_0/(gh_0)^{1/2}] = 3.92$ and 4.23. The ventilation system

provides sufficient air supply, allowing discrete air bubbles to be generated successively from the wedged tip of air cavity and then entrained into the high-speed water stream of sliding jet, forming an aerated chute flow.

3. Results and Discussions

3.1. Approach Flow as Well as Free and Sliding Jet

The feature of the approach flow upstream the offset highlights increase of U_0 (i.e., its positive convective acceleration) and the corresponding decrease of h_0 . The offset acts like a drop structure such that the change of the approach flow into a projecting free jet commences near the brink of the offset, around which depression of the free surface occurs (Lin et al. [34,38,45–47]). Detailed velocity field and profiles of the approach flow and free jet for $-4.0 \text{ cm} \leq X \leq 9.0 \text{ cm}$, along with the mass-conservation check using 2D continuity equation, is found in Lin et al. [38].

As shown in Figure 4, the free jet is a high-speed supercritical stream with the Nappe having prominent irregular fluctuations in its lower and upper free surfaces. The first water–air interface is between the atmosphere and the upper jet surface. The second exists between the lower jet surface and the upper boundary of air cavity. The third is between the lower air cavity boundary and the (upper) surface of the recirculation flow. The farthest downstream portion of air cavity is shaped like a wedge, with irregular streamwise and transverse oscillations, thus leading to drastic change in the instantaneous position of the its wedged tip. Under such a condition, the sliding jet from the free jet is generated downstream the wedged tip of air cavity (the mean position is at $X = X_{mwt} = 12.7 \text{ cm}$, to be illustrated later), where shedding of air bubbles takes place (Figure 4). Then the shed air-bubbles are entrained into the water stream of the sliding jet, resulting in the two-phase chute flow. The sliding jet, accompanied by entrained air bubbles, moves farther downstream and next impinges upon the chute surface at the instantaneous impingement point (the mean location is situated at $X = X_{mip} = 15.05 \text{ cm}$, to be further stated later). Because of the flow impingement, flow bifurcation takes place at the impingement point. Herein, one supercritical two-phase stream moves further downstream and the other minor stream is deflected upstream with a tiny amount of entrained air bubbles, thereby forming the recirculation flow. The sliding jet also exhibits more pronounced fluctuations with high frequency in the free surface (Shi [48]).

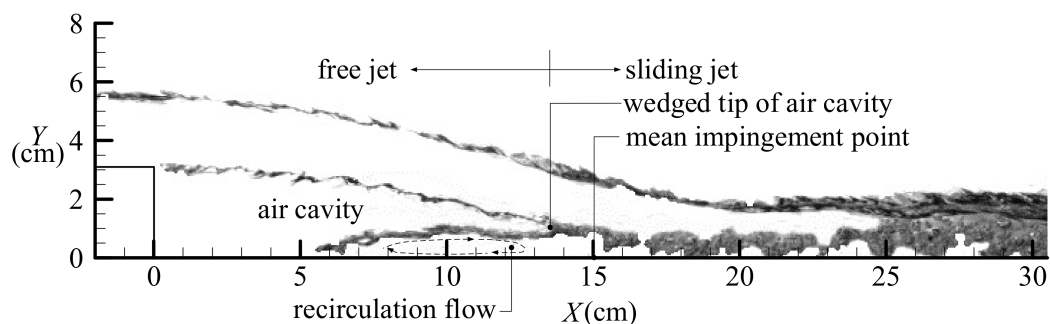


Figure 4. A global view of superposing three instantaneous SIM images captured in the FOVS₁.

It is appropriate to first demonstrate the time series of the streamwise and transverse fluctuating velocities of water stream, and then to introduce the mean velocity profiles upstream the mean wedged tip of air cavity (at $X_{mwt} = 12.7 \text{ cm}$), thus enhancing the understanding for free jet's transformation into the sliding jet (which is first characterized by riding over the recirculation flow zone). As seen in Figure 5a,b, the time histories of the streamwise and transverse fluctuating velocities, $u_w(t)$ and $v_w(t)$, obtained at $(X, Y) = (11.6, 1.63) \text{ cm}$, show very prominent random fluctuations, together with the corresponding mean velocities being $U_w = 192.5 \text{ cm/s}$ and $V_w = -45.8 \text{ cm/s}$. The auto-correlation

functions of $u_w(t)$ and $v_w(t)$, representing the averages of the products of these quantities at time t with the counterparts at time $(t + \tau)$ (Bendat and Piersol [49]), are

$$R_{uu,w}(\tau) = 1/T_{sd,w} \cdot \int_0^{T_{sd,w}} u_w(t) \cdot u_w(t + \tau) dt \tag{5}$$

$$R_{vv,w}(\tau) = 1/T_{sd,w} \cdot \int_0^{T_{sd,w}} v_w(t) \cdot v_w(t + \tau) dt \tag{6}$$

in which τ is the time lag and $T_{sd,w}$ is the sampling duration per run (= 2.25 s with a 4000 Hz sampling rate for the HSPIV measurements of the water stream). The calculation results of these two non-dimensional autocorrelation functions, defined as $R_{uu,w}^*(\tau) = R_{uu,w}(\tau)/R_{uu,w}(0)$ and $R_{vv,w}^*(\tau) = R_{vv,w}(\tau)/R_{vv,w}(0)$, are shown in Figure 5c,d. The integral time scales of $u_w(t)$ and $v_w(t)$ for the water stream, representing the largest time interval, within which the fluctuating velocity data are still interrelated, can be determined from the following two equations (Tennekes and Lumley [50])

$$T_{its,u_w} = \int_0^{\tau_{max}} R_{uu,w}^*(\tau) d\tau \tag{7}$$

$$T_{its,v_w} = \int_0^{\tau_{max}} R_{vv,w}^*(\tau) d\tau \tag{8}$$

where τ_{max} is the maximum time lag with $R_{uu,w}^*(\tau_{max}) = 0$ and $R_{vv,w}^*(\tau_{max}) = 0$. Accordingly, the two integral time scales are estimated to be $T_{its,u_w} = 0.0014$ s and $T_{its,v_w} = 0.0012$ s, highlighting their very tiny values with the order of $O(10^{-3})$ s. It is clearly found that $T_{sd,w} = 1607 \times T_{its,u_w} = 1875 \times T_{its,v_w}$ demonstrates that the sampling duration per run $T_{sd,w}$ is far larger than T_{its,u_w} and T_{its,v_w} . Note that three repeated runs were performed for the HSPIV measurements with a total sampling time of 6.75 s (i.e., with a total of 27,000 samples), thus the mean velocity characteristics of the water stream can be assured due to the total sampling time $3T_{sd,w} (= 4821T_{its,u_w} = 5625T_{its,v_w})$, being very much greater than T_{its,u_w} and T_{its,v_w} .

Furthermore, as the other supporting evidence, the mean velocity profiles obtained herein are also compared with those previously measured with six repeated runs having a total sampling time of 13.50 s ($2.25 \text{ s} \times 6$) but not shown in Lin et al. [38]. Figure 5e–g,h–j present these two sets of data points for the distributions of the mean streamwise and transverse velocities of water stream, $U_w(Y)/V_w(Y)$, measured at $X = 11.00, 11.60,$ and 12.2 cm, respectively. Good agreement exists between these two data trends, highlighting repeatability of the mean flow characteristics of water stream and the convergence of the mean velocity characteristics. Note that the central parts of the three mean velocity profiles of either $U_w(Y)$ or $V_w(Y)$ are, in fact, fairly uniform. The uniform streamwise velocities demonstrated in Figure 5e–g are identified to be $U_{wu} = 238.3, 237.6$ and 234.4 cm/s, respectively, exhibiting a slight decrease in U_{wu} with an increase in X .

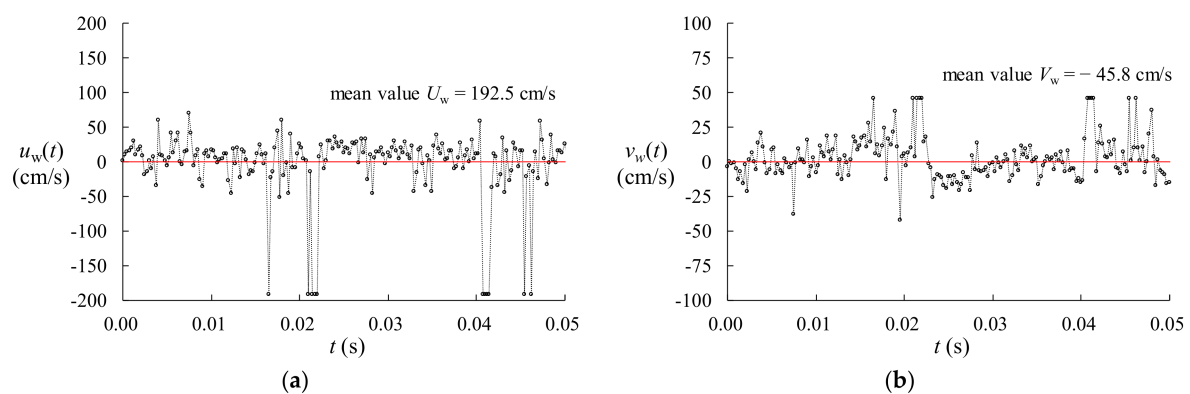


Figure 5. Cont.

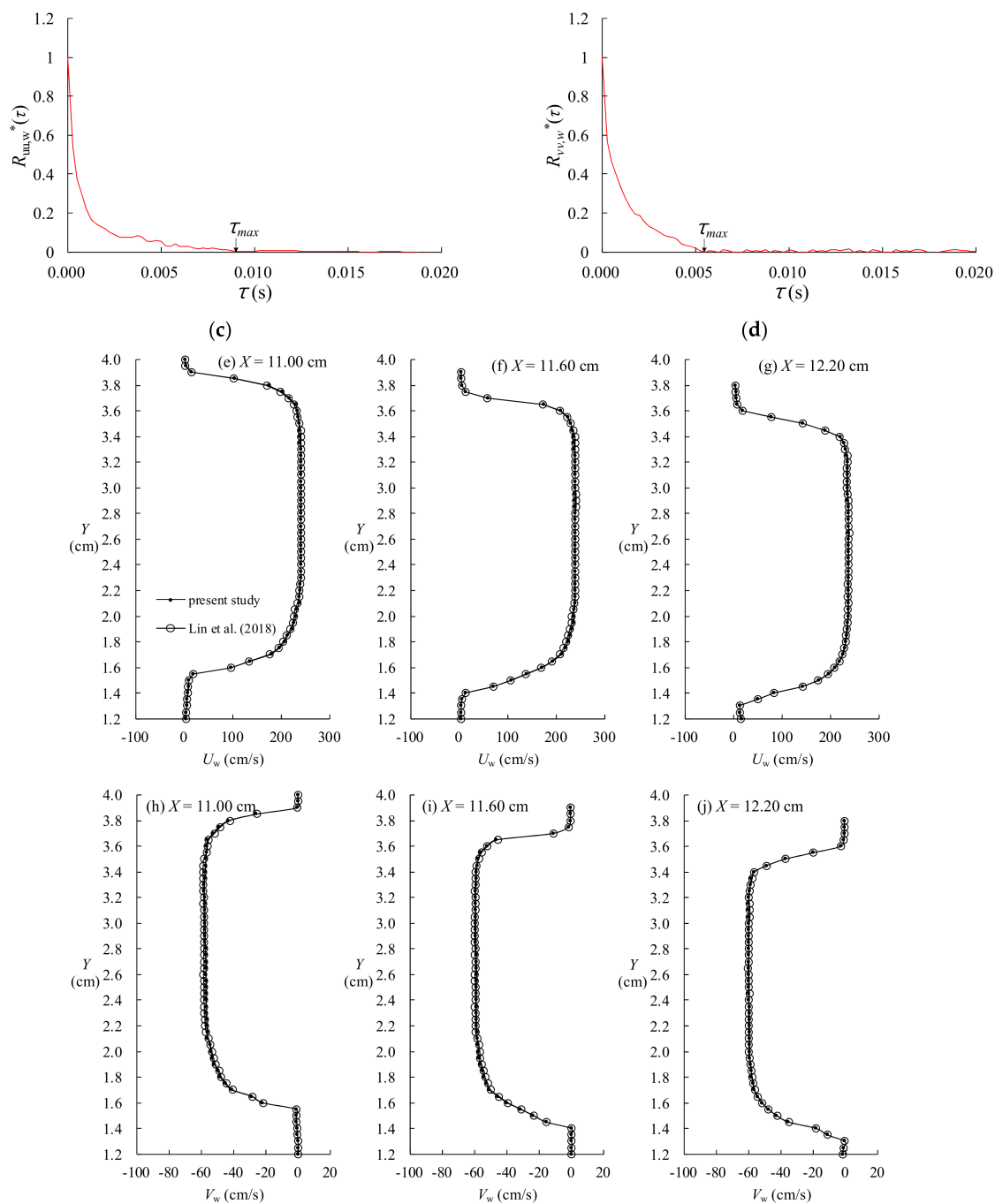


Figure 5. (a,b) The time histories of the streamwise/transverse fluctuating velocity $u_w(t)/v_w(t)$, obtained at $(X, Y) = (11.6, 1.63)$ cm; (c,d) The non-dimensional autocorrelation function $R_{uu,w}^*(\tau)$ and $R_{vv,w}^*(\tau)$ for the water stream. The mean streamwise/transverse velocity profile of water stream of the free jet obtained at three different sections: (e,h) $X = 11.00$ cm; (f,i) $X = 11.60$ cm; (g,j) $X = 12.20$ cm.

However, the uniform transverse velocities underlying Figure 5h–j are determined to be $V_{wu} = -57.4, -59.2,$ and -60.1 cm/s, respectively, indicating small increase in the magnitude of V_{wu} with increasing X . In other words, prior to occurrence of the sliding jet at $X_{mwt} = 12.7$ cm, the decrease of mass or momentum in the streamwise direction has been correspondingly transferred into the increase of counterpart in the negative transverse direction. Following the mass-conservation calculation procedure adopted in Lin et al. [35,38], a detailed check in the flux of each grid element $f = | \partial U_w / \partial X + \partial V_w / \partial Y | dA$ (in which $\Delta X = \Delta Y = 0.41$ mm is used and $dA = \Delta X \times \Delta Y$ is the area of

a grid element) is performed in the corresponding velocity field (not shown). The relative error of the flux in the velocity field can be defined as f/f_0 (where $f_0 = U_{wu} \times \Delta Y$). Note that the values of f/f_0 at most positions with low velocity gradient are less than 1.6%, and the counterparts at locations having prominent velocity gradient zone are no greater than 3.4%, confirming precise HSPIV measurements of the mean velocity field for $11.0 \text{ cm} \leq X \leq 12.5 \text{ cm}$ (i.e., further downstream of free jet before entering the reach of sliding jet).

It is pertinent to note that, at $X = 0 \text{ cm}$, the streamwise velocity profile of the approach flow shows a boundary layer thickness of about 0.65 cm over a water depth of 2.62 cm [38], indicating that the approach flow is not fully developed. For $0 \text{ cm} < X < 9.0 \text{ cm}$ in Lin et al. [38] and for $X = 11.0\text{--}12.2 \text{ cm}$ in Figure 5e–g, the free jet features the fairly uniform streamwise velocity distributions, which may be in all likelihood attributable to the non-fully developed situation of the approach flow. However, uniform velocity profiles of a free jet were reported by Rajaratnam and Chamani [51] (see their Figure 3) for a fully developed approach flow upstream of a drop structure. Accordingly, the uniform velocity distributions of the free jets are evidenced without regard to the two distinct approach flow conditions.

3.2. Removal of Noise-Like Blurred Background and Foreground with Low Gray-Levels in SIM Images

It is worth noting that, during the SIM experiments, the use of special lens allows the water–air interfaces and air-bubble contours only within the DOF to be captured clearly in the images. However, due to overlapping of the water–air interfaces and air bubbles appearing outside the DOF, mainly between the focal plane and the rear step-shaped vertical plate with the air slot, the corresponding noise-like blurred background with fairly low gray levels are seen in the recorded images. For examples, Figure 6a,b shows two instantaneous magnified views with relatively dark but blurred-background regions, which are superposed upon the images captured within the DOF. The two instantaneous moments, $t = -0.15866$ and -0.15833 s , shown in Figure 6a,b are identified with reference to $t = 0$.

It becomes thus necessary to remove the noise-like blurred background appearing outside the DOF. Herein, an image processing method used by Zhou et al. [52] and Sonka et al. [53] is mainly adopted. The procedure is briefly demonstrated as follows:

- (1) To input the gray-level values identified at all of the ‘pixel points’ for two arbitrary neighboring images (e.g., Figure 6a,b);
- (2) To smooth the gray-level values of these two images using Gaussian core function (Catt et al. [54]) with 7×7 pixels (e.g., Figure 6c,d corresponding to Figure 6a,b);
- (3) To calculate the differences in the gray levels of these two ‘smoothed images’ and then acquire the corresponding ‘difference image’, from which the absolute value of the gray-level difference at each pixel point is obtained (Figure 6e);
- (4) To extract the preliminary outline of two-phase flow image from (3) employing the active-contour technique developed by Chen and Vese [55], in which the region-based energy model with the initial seed mask for the absolute value of the gray-level difference being greater 10 is specified. Accordingly, the preliminary segmentation for the ‘binary image’, which holds the value of either the unity or zero at each pixel point, is realized (see Figure 6f). Note that the unity (with white color)/zero (with black color) in the binary image, in fact, stands for the water–air interface and air-bubble contour/the water stream of jet and the atmosphere.
- (5) To apply various morphological processing skills to deal with the binary image obtained (Gonzalez et al. [40]), including the filling, dilation, erosion, closing and opening operations:
 - ① The closing operation is performed using a disk-shaped mask with a radius of 8 pixels (Figure 6g);
 - ② The filling operation is then executed to fill the holes in the image by using a square structural element with its center being linked to the neighboring 4 connected pixels (see Figure 6h);

- ③ A threshold of area less than 100 pixels² is utilized to remove the small pixel area for all the isolated objects (Figure 6i);
 - ④ The dilation operation is then carried out using a disk-shaped mask with a radius of 5 pixels (see Figure 6j);
 - ⑤ The erosion operation is done using a disk-shaped mask with a radius of 3 pixels, aiming to remove redundant pixel from the contours of air bubbles for smoothing the boundaries (Figure 6k);
- (6) To obtain the image with clear gray-level contours of both water–air interfaces and air bubbles, in which the noise-like blurred background eventually gets filtered out (see Figure 6l);
- (7) To repeat all of the steps from (1) through (6) to acquire the time series of the processed images, in which only clear gray-level contours of the water–air interfaces and air bubbles are highlighted.

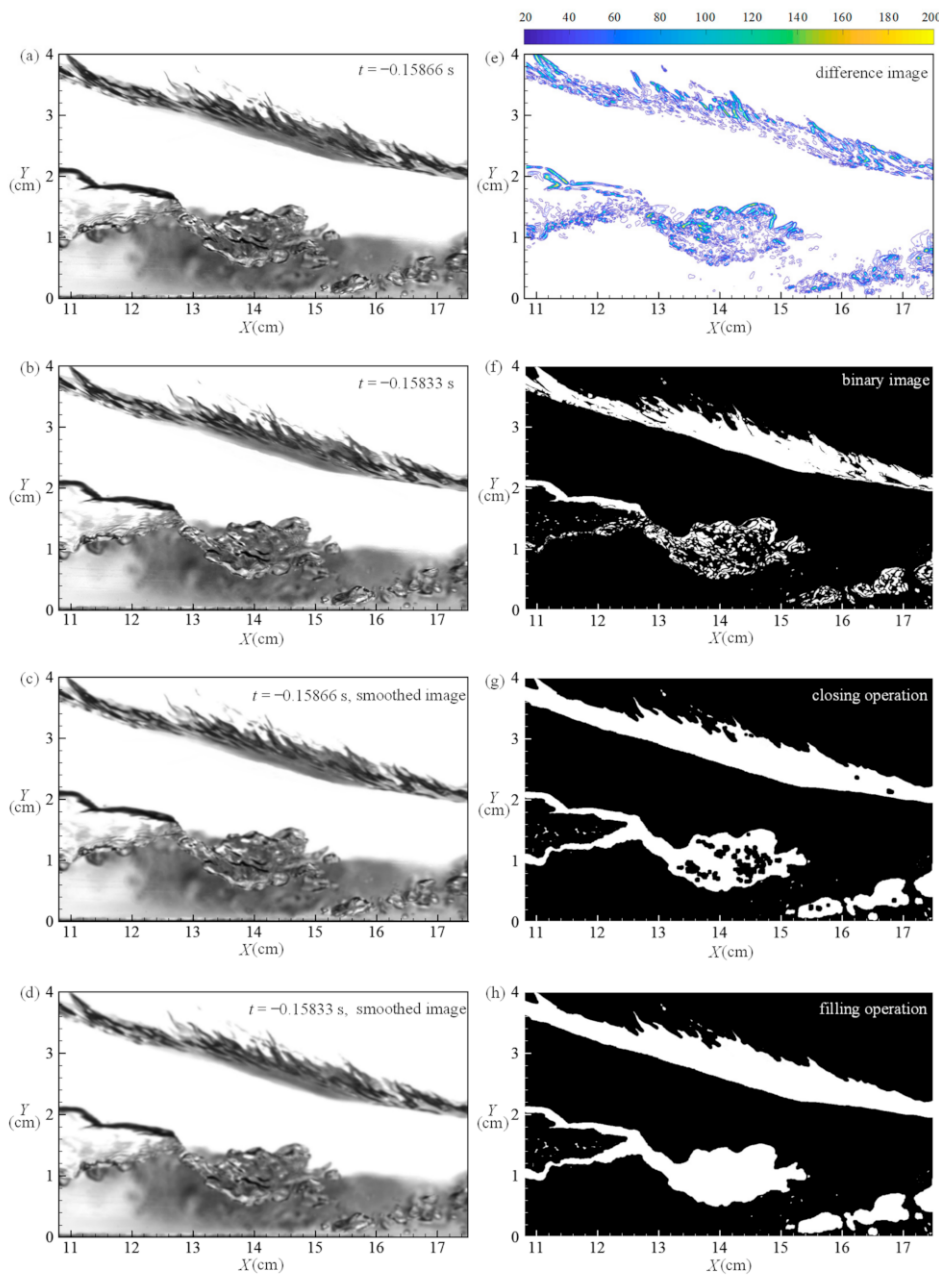


Figure 6. Cont.

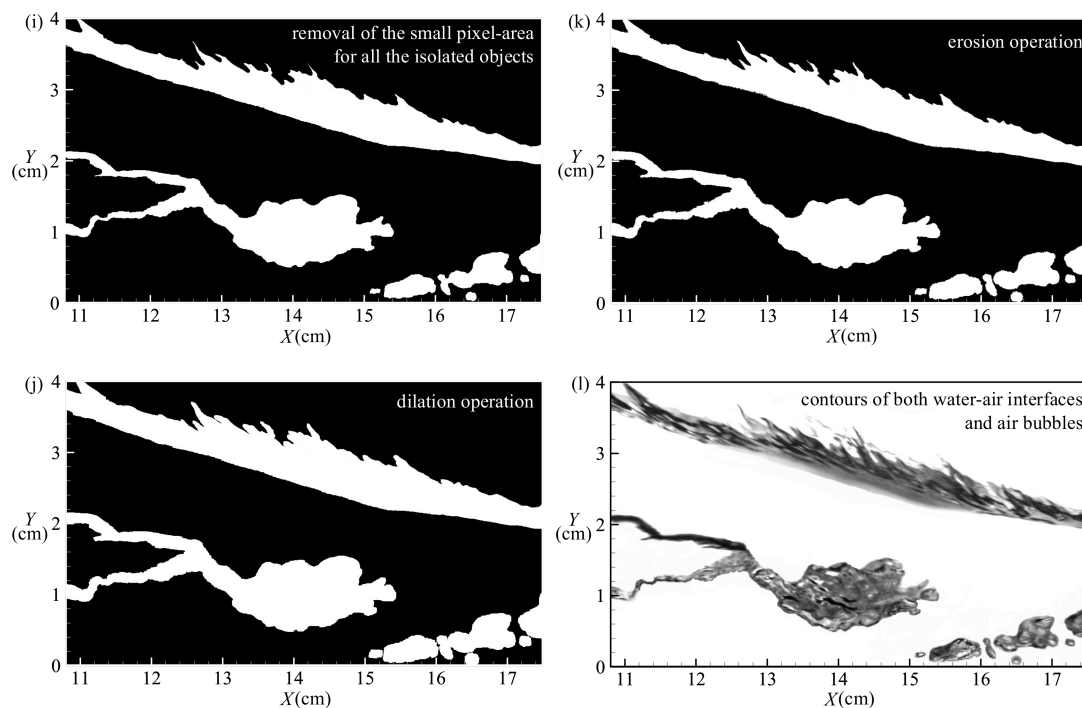


Figure 6. (a,b) The instantaneous magnified image exhibiting relatively dark, noise-like blurred background appearing outside the DOF at $t = -0.15866$ s/ -0.15833 s; (c,d) The smoothed image corresponding to (a,b); (e) The difference image obtained from (c, d), along with the color code representing the difference in gray-level; (f) The binary image acquired; (g) The image procured by closing operation; (h) The image achieved by filling operation; (i) The image obtained by removal of the small pixel-area for all the isolated objects; (j) The image obtained by dilation operation; (k) The image given by erosion operation; (l) The processed image with clear gray-level contours of both water-air interfaces and air bubbles (i.e., the noise-like blurred background has been effectively removed).

Similarly, due to overlapping of the water–air interfaces and air bubbles taking place outside the DOF and between the focal plane and the front glass wall (with a separation of 9.0 cm), the effect of the noise-like blurred foreground with low gray levels can be evaluated as follows:

- (1) To set the center of the focal plane 9.0 cm away from the inner surface of the front glass wall;
- (2) To record the relatively clear SIM images accompanied by the noise-like blurred-background images in the FOVS₂;
- (3) To display the time series of the relatively clear images with the blurred background, e.g., as the magnified view shown in Figure 7a;
- (4) To remove the blurred background following the image processing steps employed for Figure 6a–l, thus only allowing the image with clear air-bubble contours to be left behind (see Figure 7b);
- (5) To adjust the center of the focal plane on the inner surface of the front glass wall;
- (6) To capture the ‘blurred-foreground’ SIM images for air bubbles moving downstream between the focal plane and the inner surface of the front glass wall in the FOVS₂;
- (7) To demonstrate the time series of the blurred-foreground images (e.g., one of the images is seen in Figure 7c);
- (8) To superpose the time series of the clear air-bubble images and the blurred-foreground images from the above steps (4) and (7), e.g., one of the superposed images is presented in Figure 7d;
- (9) To utilize again the image processing procedure (as employed in Figure 6a–l) to the superposed images;
- (10) To obtain the time series of the post-processing images (one of the examples is shown in Figure 7e).

It is thus found that the post-processing image obtained in step (10) (i.e., Figure 7e) is almost identical to the counterpart with the blurred background being filtered (see Figure 7b), highlighting that the blurred-foreground images are effectively removed and only the targets inside the DOF are clearly identified. This evidence also confirms that the blurred-foreground images hardly have the overlapping effect on the filtered images captured in the DOF and on the corresponding velocity fields obtained by the BIV analysis (discussed later in Section 3.6).

In the following, only the images with removal of noise-like blurred background and foreground are used for further analysis.

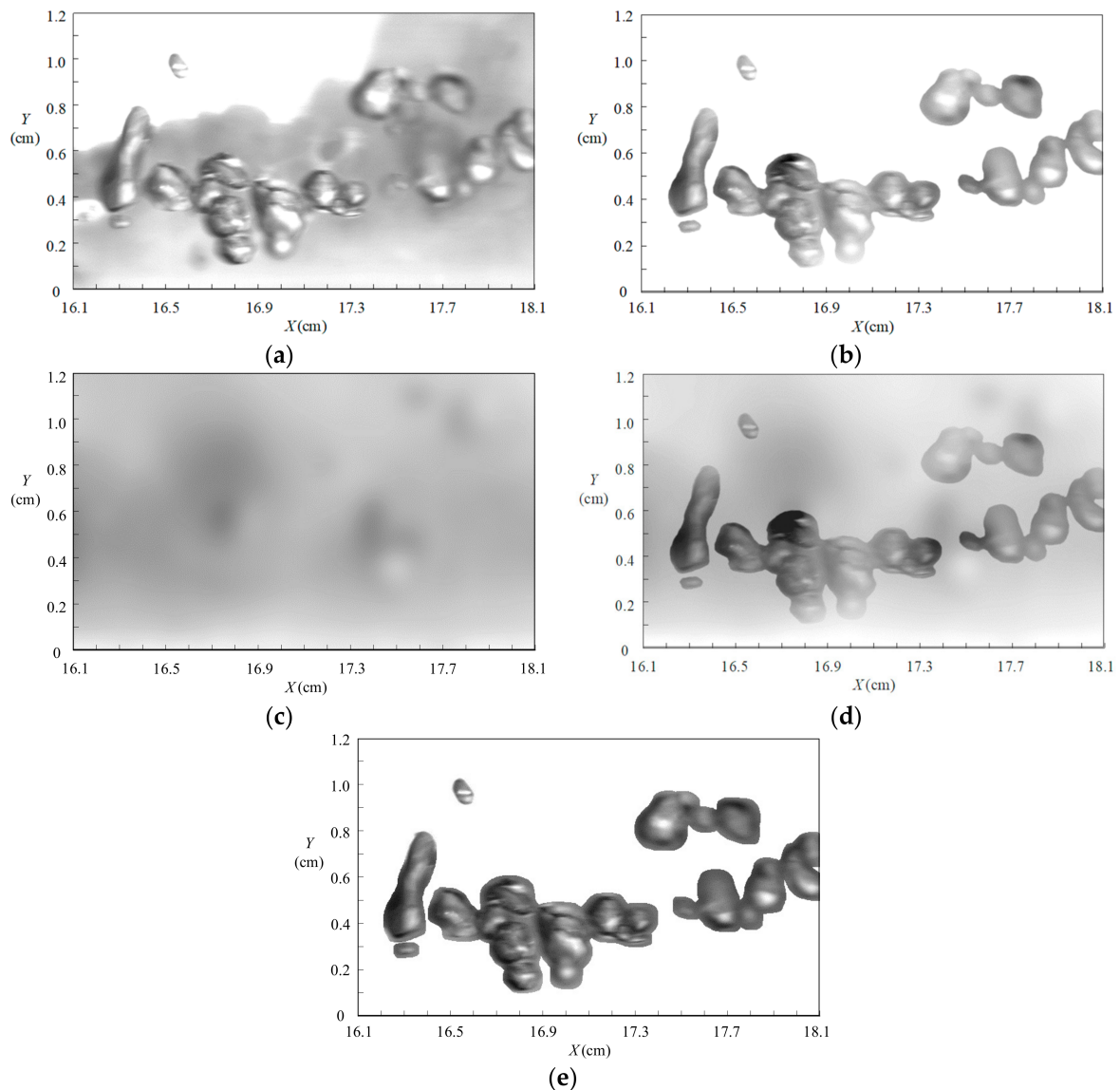


Figure 7. An example of the magnified image illustrating effective removal of the blurred-foreground: (a) Relatively clear image captured in the DOF mainly accompanied by the blurred-background image with fairly low gray level; (b) Clear air-bubble image captured in the DOF with the blurred background being removed; (c) Blurred-foreground image taken between the front glass wall and the center of the focal plane; (d) Superposed image consisting of the clear air-bubble (b) and the blurred-foreground (c) images; (e) The image left behind with removal of the blurred foreground via the image processing steps employed for Figure 6a–l, demonstrating this image is nearly the same as that shown in (b).

3.3. Shedding Process of Air-Bubbles from Wedged Tip of Air Cavity

Based on the preliminary observations from the flume bottom, the wedged tip of air cavity mainly exhibits the two-dimensional feature with slightly random wavy oscillation without evident shock-wave-like characteristic (see Figure 8a,b). After examinations, the mean values of the streamwise positions for the wedged tip of air cavity in the spanwise direction are nearly equal to $X_{mwt} = 12.7$ cm with slight variation of ± 0.12 cm for $-5.0 \text{ cm} \leq Z \leq 10.0 \text{ cm}$. As a further supporting witness, the air-bubble concentration distribution (measured at $(X, Y) = (13.4, 1.4)$ cm by using fiber-optic reflectometer in Li [41]) is found to be fairly uniform in the spanwise direction for $-1.0 \text{ cm} \leq Z \leq 12 \text{ cm}$. These two evidences strongly highlight the two-dimensional feature of the mean position for the wedged tip of air cavity and are independent of the spanwise location of interest. Accordingly, in the following, the observation results for evolution of air bubbles generated from the wedged tip of air cavity are only focused on the DOF at 9.0 cm away from the inner surface of the front glass wall (i.e., at $Z = 0$ cm).

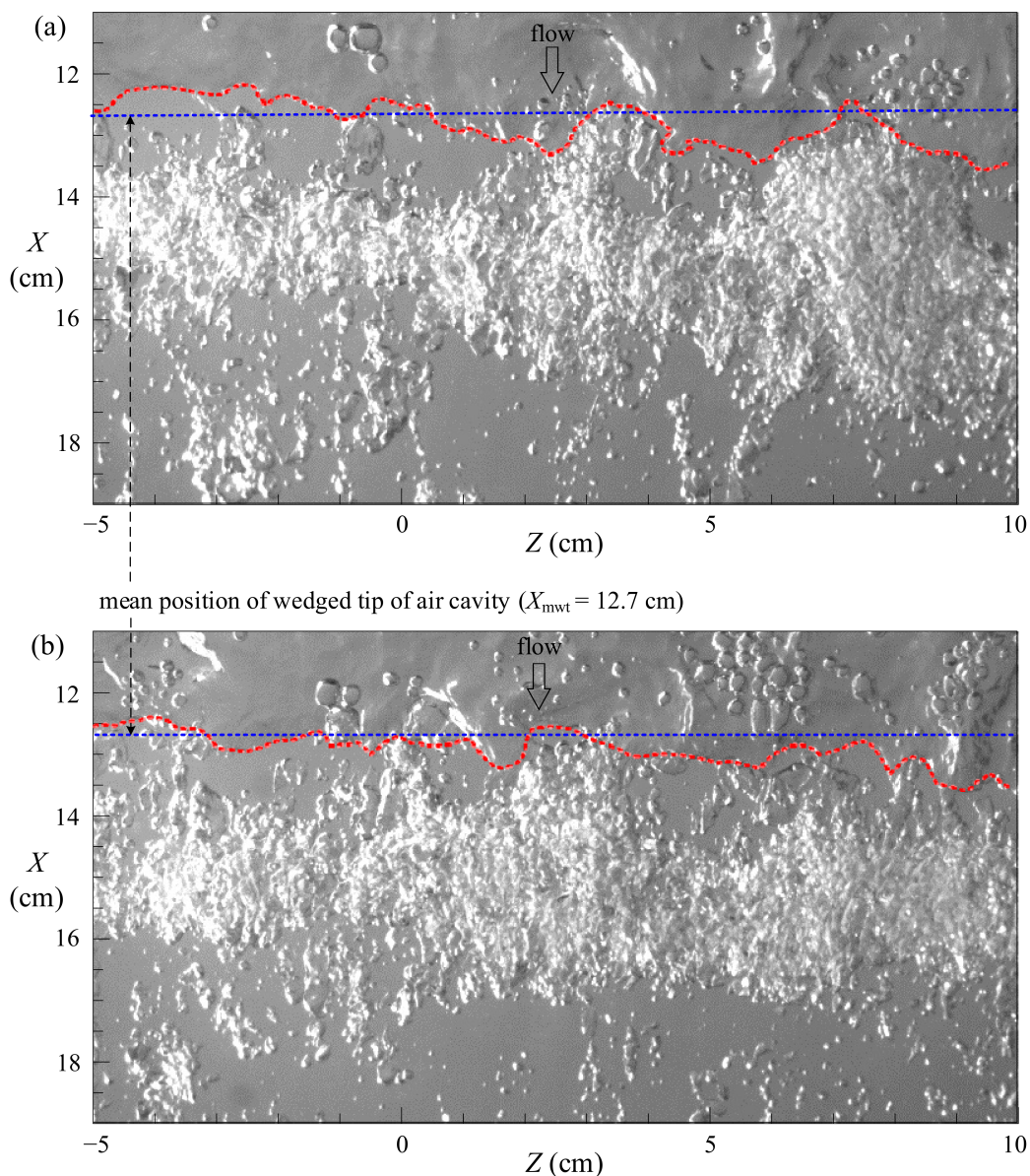


Figure 8. Two snapshots showing wavy variation in the instantaneous position of the wedged tip of air cavity (marked in red curve) in the spanwise direction, together with indication of the mean location (beveled with blue dashed line).

More detailed flow observations around the wedged tip of air cavity within the FOVS₂ reveal that air-bubbles are produced and then shed mainly by one of the following ways. Firstly, the air-bubbles, as marked by A in Figure 9a–c, are shed from a whole wedged tip of air cavity *without branching* (for the reference time t varying from 0, via 0.002, to 0.004 s) due to the action of high shear between free jet and air cavity as well as fluctuating wavy motion of the lower free surface of free jet. Herein, the time interval between the end of a complete shedding of previous air-bubbles and the counterpart of a next one can be defined as the *time duration* of an entire shedding process, t_d . As observed and estimated from the visualized images (with a 3000 Hz framing rate), the time duration for air-bubbles A is $[t_d]_A = 0.00533$ s. As also seen in Figure 9a–c, three clusters of air-bubbles (as marked by O, O' and O'') shed previously from the wedged tip of air cavity keep moving downward with successive deformation but without evident lifting motion. Such deformation can be attributable to the rotation and/or elongation motion coupled not only with collision and/or amalgamation between the neighboring air bubbles, but also with disintegration of larger air bubble(s) into several smaller air bubbles.

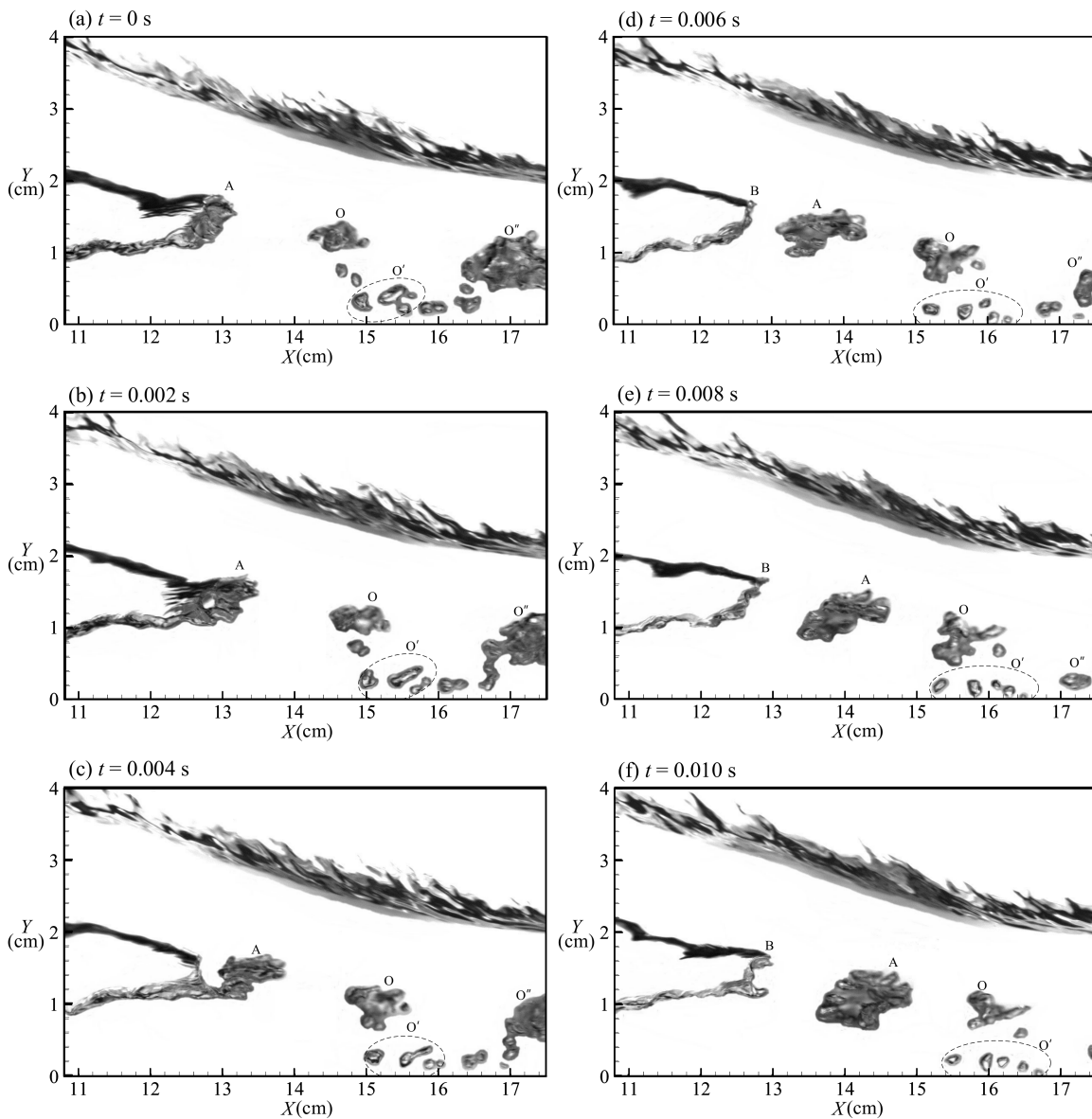


Figure 9. Cont.

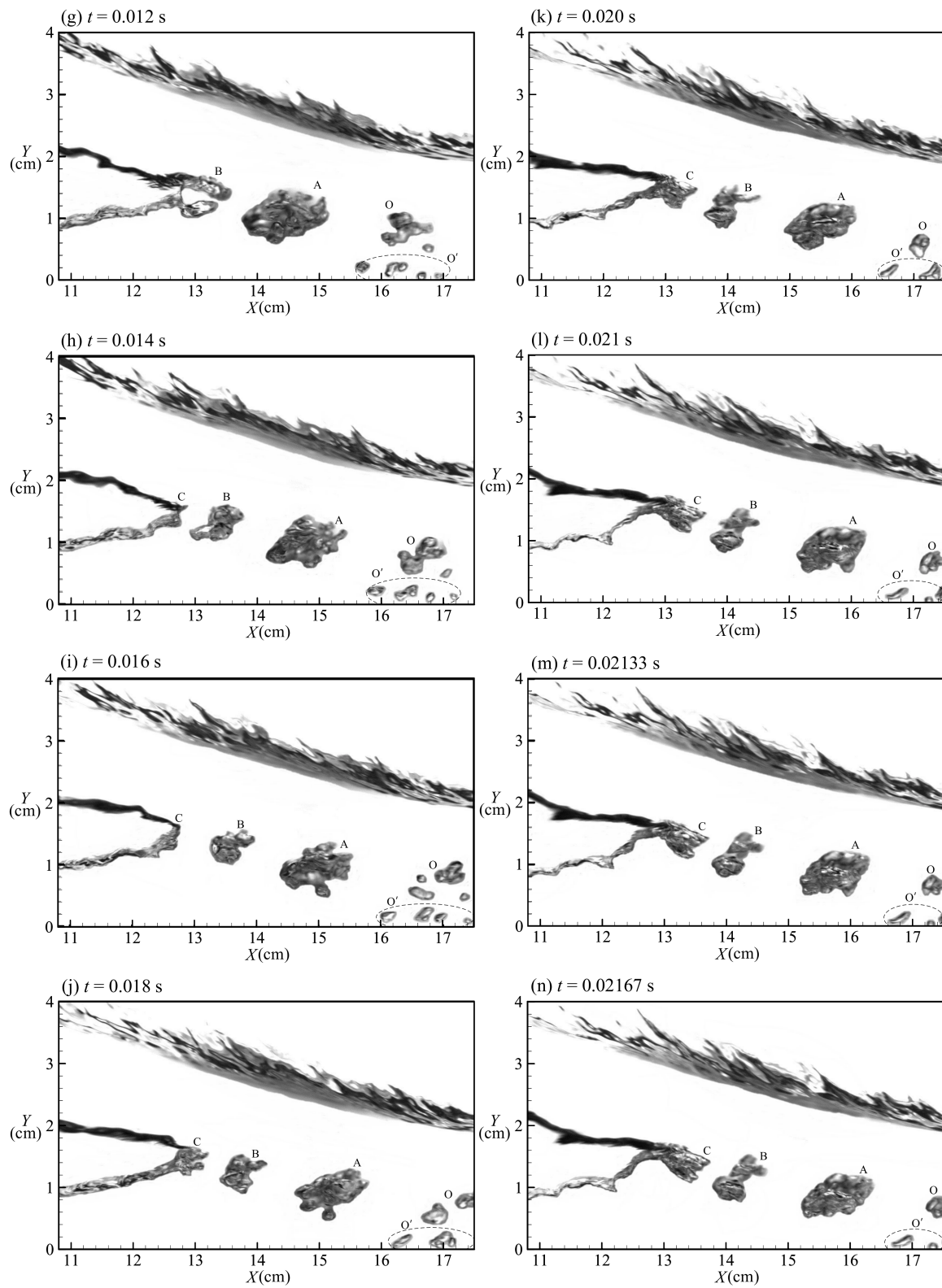


Figure 9. Cont.

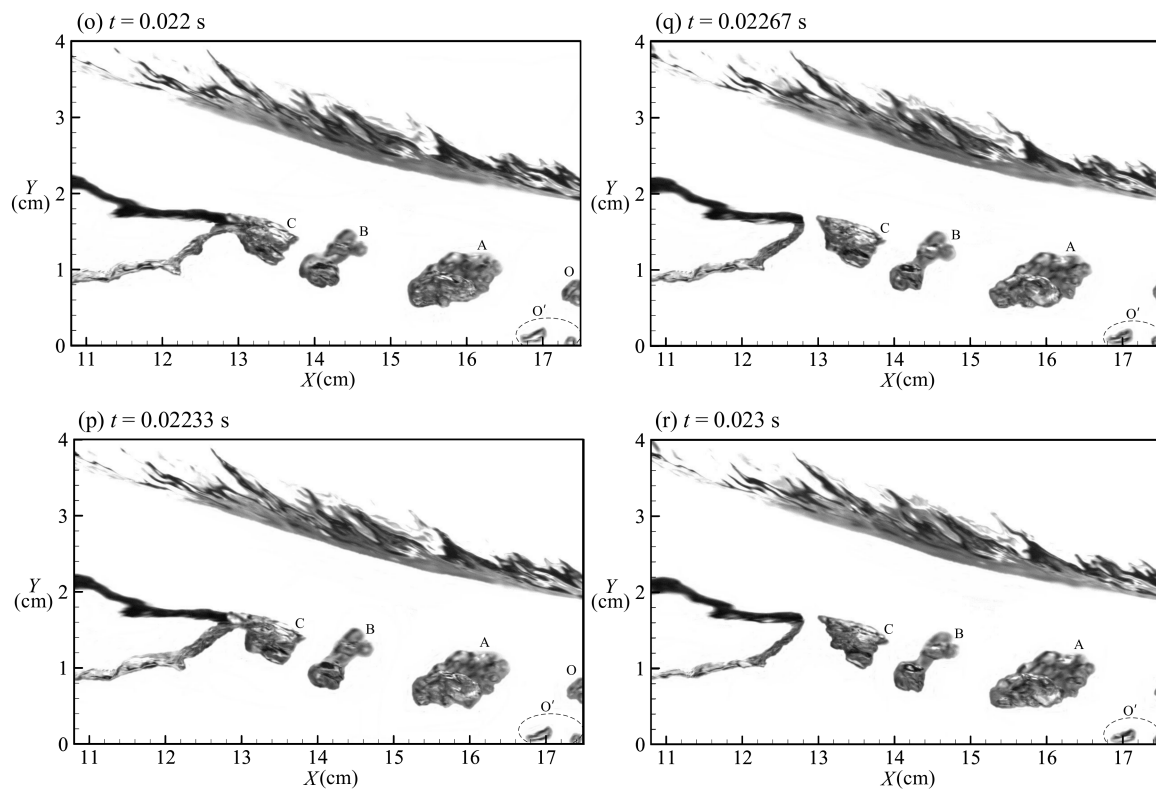


Figure 9. Time series of the instantaneous SIM images after removal of the blurred background, showing that air bubbles are released: (a–c) sequentially from a whole wedged tip of air cavity without branching; (d–h) simultaneously from different finger-like branches at the wedged tip of air cavity; (i–r) via the formation of relatively convergent wedge-shaped tip from which the air bubbles are generated directly.

Secondly, the shedding process can be also achieved by means of releasing simultaneously from “fingering” at the wedged tip of air cavity. The fingering at the wedged tip is observed prior to the shedding of air-bubbles, along with considerably fluctuating wavy boundary between the free jet and the upper surface of air cavity. This means that the whole wedged tip is subjected to prominent fluctuating force and shear, exerting stress on the wedged tip and then making the whole one deformed into a complex wedged tip with at least two finger-like branches (at different positions). Such a shedding process with branching from the upper and lower edges of the wedged tip (as labeled by B) can be evidenced in Figure 9d–h for t ranging from 0.006 to 0.014 s with the time interval between two neighboring images being equal to $\Delta t = 0.002$ s. Prominent elongation or stretching of the wedged tip of air cavity along with oscillation of the wavy boundary between the free jet and the upper surface of air cavity can be seen clearly. The time duration for this shedding event is $[t_d]_B = 0.00967$ s. The shed air bubbles B is then transported downstream, similar to the behavior of air bubbles A, together with the rotation and/or elongation motion being combined mainly with: (1) collision and/or merging with neighboring air bubbles; (2) disintegration of larger air bubble(s) into smaller air bubbles; and (3) both mentioned in (1) and (2).

The third way of the shedding process is via the formation of relatively convergent wedge-shaped tip from which the air bubbles are shed directly. Such an example can be witnessed in Figure 9i–r with t changing from 0.016 s to 0.023 s for the shedding process of the third cluster of air bubbles (as marked by C). For highlighting the detailed evolution of the air bubbles C disconnecting from the wedged tip of air cavity, a series of images starting from $t = 0.021$ s to $t = 0.023$ s are particularly shown in Figure 9l–r with $\Delta t = 1/3000$ s. The time duration for this shedding event is $[t_d]_C = 0.009$ s. Furthermore, from the observation through a series of images, certain air bubbles may move faster towards downstream and

then catch up with the previously released ones, thus resulting in the interaction of air bubbles, with air bubble coalescence and/or breakup.

By visual counting of the time elapse between two adjacent shedding processes from continuous record of 3000 images captured in the FOVS₂ for over 100 shedding events, it is found that the averaged time duration for the “shedding” process of air bubbles generated at the wedged tip is estimated to be $[t_d]_{ave} = 0.0102$ s, along with a maximum of $[t_d]_{max} = 0.0323$ s and a minimum of $[t_d]_{min} = 0.001$ s for the present case. It is worth mentioning that, for a steady jump with the approach-flow water depth of 1.91 cm and a Froude number of 4.51 (Lin et al. [35]), the averaged time duration for the “entraining” process of air bubbles from the (upstream) tip of the surface roller of the jump into the its toe is estimated to be $[t_d]_{ave} = 0.025$ s, larger than the value ($=0.0102$ s) of the present study.

Moreover, Figure 10 presents a magnified view for the superposed edition of three instantaneous images for $8.0 \text{ cm} \leq X \leq 30.0 \text{ cm}$, taken partly from the FOVS₁ (for $-0.2 \text{ cm} \leq X \leq 30.5 \text{ cm}$). For $12.7 \text{ cm} \leq X < 18.5 \text{ cm}$, air bubbles are carried downstream rapidly by the sliding jet with prominent *downward motion*. Namely, the air bubbles mainly exist in the lower part of the water stream of the sliding jet. Some air bubbles carried by the high-speed water stream can move more downward and then impinge upon the chute surface around the instantaneous impingement point, thus resulting in evident disintegration of air-bubble cluster into more discrete air bubbles for $X < 18.5 \text{ cm}$. However, for $X > 18.5 \text{ cm}$, the air bubbles sustained still move toward downstream but with evident *lifting motion*, which is induced by the buoyancy force. As witnessed in Figure 10, lifting of air bubbles becomes more prominent as the observation section is located more downstream the demarcation point at $X = 18.5 \text{ cm}$.

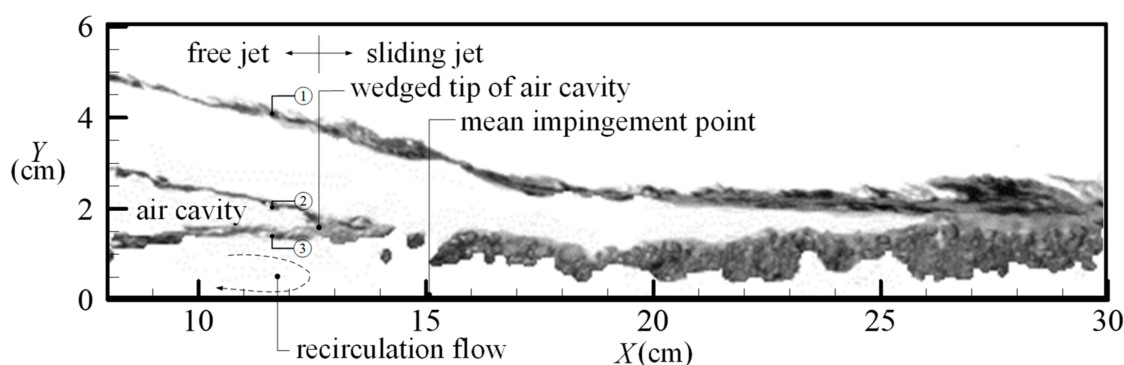


Figure 10. A magnified view for superposing three instantaneous SIM images taken partly from those captured in the FOVS₁ with removal of the blurred background.

3.4. Characteristics of Instantaneous and Ensemble-Averaged Gray Level Distributions of SIM Images

Figure 11a shows one of the *instantaneous gray level distributions* (IGLD, as marked by “dotted line”) in the SIM images at $X = 11.40 \text{ cm}$ within the interval $0 \text{ cm} \leq Y \leq 4.4 \text{ cm}$. For $Y > 3.82 \text{ cm}$ and $2.0 \text{ cm} < Y < 3.50 \text{ cm}$, full air phase emanating from the atmosphere and full water phase from the free jet appear, respectively. This situation leads to the instantaneous gray level equal to $G = G_{max1} = G_{max2} = 255$ (i.e., the maximum value that corresponds to the *lightest* gray level). However, for Y decreasing from 3.75 to 3.65 cm and $3.50 \text{ cm} \leq Y \leq 3.65 \text{ cm}$, significant decrease of the gray level from $G_{max1} = G_{max2} = 255$ to the first local minimum $G_{min1} = 41$ is clearly witnessed. This is attributable to the ‘shadow effect’ caused by existence of the first water–air interface between atmosphere and free jet, allowing in determining its instantaneous position. As the height further decreases from $Y = 2.0$ to 1.91 cm approximately, a prominent decrease of gray level from G_{max2} down to the second local minimum $G_{min2} = 35$ is seen. This evidence reveals that the shadow effect induced by existence of the second water–air interface between the lower free surface of free jet and the upper boundary of air cavity. Furthermore, the third water–air interface is seen in the interval for $0.85 \text{ cm} < Y < 1.02 \text{ cm}$, beyond/below which the lower boundary of air cavity/the (upper) surface of the recirculation flow happens. The third local minimum

$G_{\min 3} = 53$ at $Y = 0.94$ cm highlights the instantaneous location of the third water–air interface. Some greater spike-like gray level fluctuations take place for $1.02 \text{ cm} < Y < 1.31 \text{ cm}$ due to existence of water in the gaps among neighboring air bubbles. However, a local gray-level peak, $G_{p,ac} = 255$, occurs pronouncedly for $1.31 \text{ cm} < Y < 1.85 \text{ cm}$, reflecting the approximate central part of air cavity. Note that the gray level reaches $G_{\max 3} = 255$ again for $0 < Y < 0.85 \text{ cm}$ due to appearance of nearly full water phase in the recirculation flow. Following the similar procedure mentioned above, a time series of the IGLDs for different images captured continuously for $X = 11.40 \text{ cm}$ or elsewhere can be achieved. Accordingly, the ensemble-averaged gray level distributions (EAGLDs) are obtained using a series of images.

Figure 11a also presents various EAGLDs obtained at $X = 11.40 \text{ cm}$ for the images with a total of frames varying from 200, via 1000, to 9000 (with per increase of 1000). As observed in Figure 11a, the global trend of the EAGLD for 200-frame images is very different from that of the IGLD for only one frame, exhibiting randomness of the gray level distribution for using only one frame. Furthermore, prominent distinctions among the EAGLD for the 2000-frame images and the counterparts of 1000-frame and 200-frame are observable clearly, especially around the ensemble-averaged positions from the first to the third water–air interfaces where the gray levels have the local minima. However, with increasing frame images N_1 ($=2000\text{--}8000$), the entire trend of the EAGLDs for the N_1 -frame images is more approaching to that for the 9000-frame ones. Tiny differences in the EAGLDs for the 8000-frame and 9000-frame images are nearly indiscernible, especially the ensemble-averaged positions, at which the three local minima $G_{\min i}$ ($i = 1\text{--}3$) appear, are nearly the same.

This implies that use of 8000 or 9000 images is pertinent to determine the target of convergence and the representative EAGLD. Such a feature can be also witnessed quantitatively by calculating the ‘entire standard deviation’ of the EAGLD for the N_2 -frame images (with $N_2 = 200$ and $1000\text{--}8000$) with respect to that for the 9000-frame ones. The calculation was based on each of the differences between the ensemble-averaged gray levels for the N_2 -frame images and those for the 9000-frame ones for $0 \text{ cm} \leq Y \leq 4.0 \text{ cm}$. Accordingly, the values of the entire standard deviation of gray level in the EAGLD for 200, 1000–4000, and 5000–8000 frames with respect to that for 9000 frames are estimated to be 12.3, 7.49–4.76, and 3.08–0.44, respectively. These values decrease prominently with increasing N_2 , demonstrating the errors are all less than 2.5% for $N_2 = 6000\text{--}8000$. This evidence again substantiates appropriate use of 8000 or 9000 images to identify the ensemble-averaged positions of the three water–air interfaces. As shown in Figure 11a for the 9000-frame images, the ensemble-averaged positions of the three water–air interfaces, where $G_{\min 1} = 154$, $G_{\min 2} = 110$, and $G_{\min 3} = 185$ appear, are located at $Y = 3.56$, 1.90 , and 1.11 cm , respectively. Note that these corresponding positions are all identical to those for 8000-frame counterpart. Therefore, only the EAGLD for the 9000 images obtained at distinct streamwise sections is presented in the following.

Figure 11b–f presents different EAGLDs for the 9000-frame images obtained at five sections between $X = 12.0$ and 13.0 cm . As seen in Figure 11a–c for $X = 11.4$, 12.0 , and 12.2 cm , the representative positions at which the third local minima (i.e., $G_{\min 3}$) take place just identify the locations of the third water–air interface at $Y = 1.11$, 1.27 , and 1.35 cm , respectively. Furthermore, as compared with that shown in Figure 11a, the most prominent distinction among Figure 11b–f is the drastic change of the EAGLD between $Y = 1.2$ and 2.0 cm for $X = 12.0\text{--}13.0 \text{ cm}$. Because $G_{\min 2}/G_{p,ac}$ keeps increasing/decreasing and the depth interval ΔY (between these two representative positions where $G_{\min 2}$ and $G_{p,ac}$ occur) becomes smaller. Eventually, $G_{\min 2}$ approaches to $G_{p,ac}$ and ΔY decreases to zero at $X = 12.7 \text{ cm}$. The evidence highlights convergence of the averaged geometric shape of air cavity into a wedged tip at the mean section, $X = X_{mwt} = 12.7 \text{ cm}$ (see Figure 11e), where the second water–air interface merges the third one (see Figure 11f). Meanwhile, for the lowest part of EAGLDs shown in Figure 11b–f, the gray levels reach back to $G = G_{\max 3} = 255$ in the vicinity of the chute surface due to appearance of nearly full water phase in the recirculation flow.

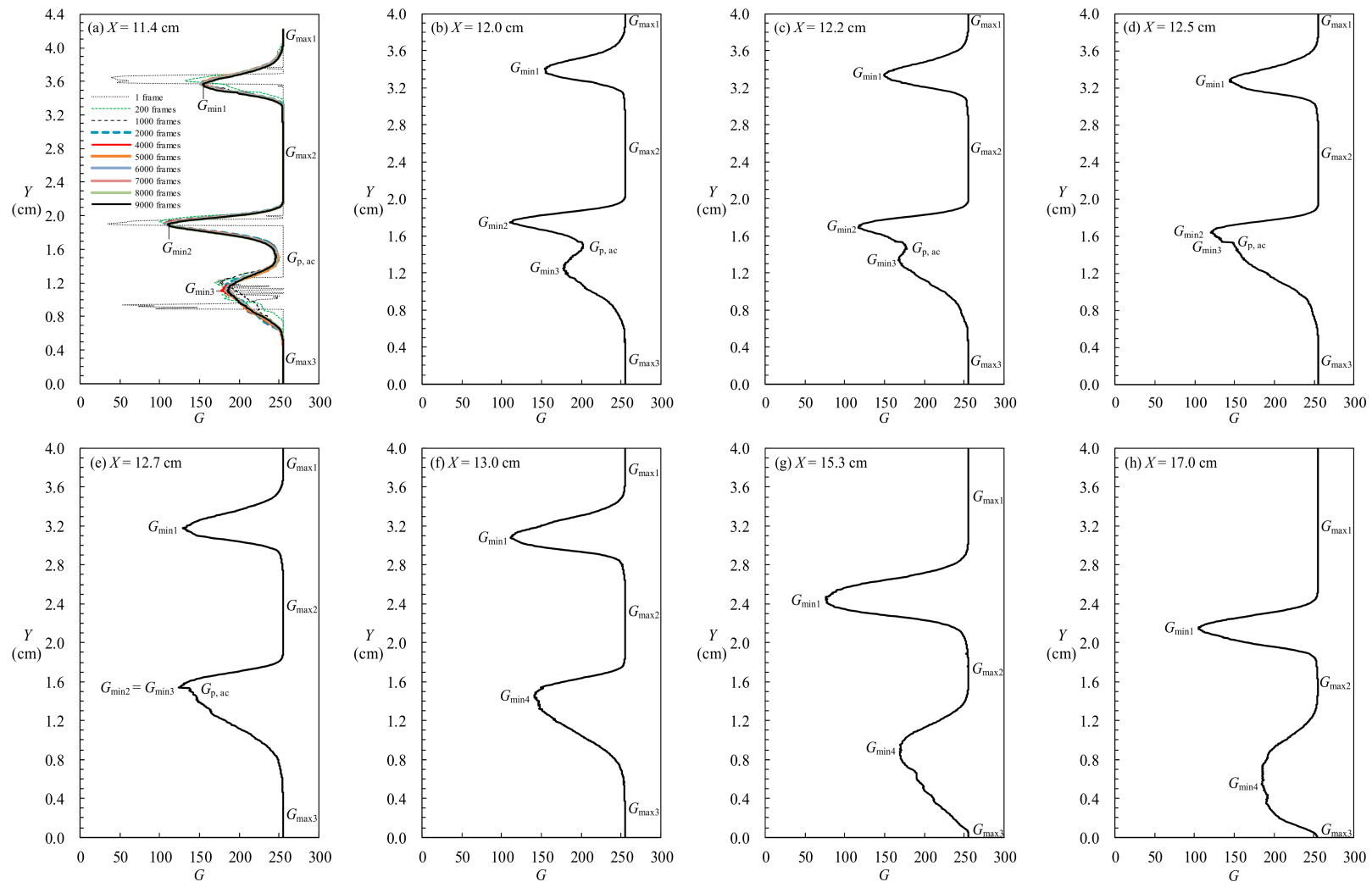


Figure 11. (a) One IGLD and several EAGLDs obtained at $X = 11.40$ cm; the EAGLD for 9000-frame images at (b) $X = 12.0$ cm; (c) $X = 12.2$ cm; (d) $X = 12.5$ cm; (e) $X = 12.7$ cm; (f) $X = 13.0$ cm; (g) $X = 15.3$ cm; (h) $X = 17.0$ cm.

In addition, Figure 11g,h illustrates the EAGLDs for the 9000-frame images at $X = 15.3$ and 17.0 cm, respectively, which are both located downstream the wedged tip of air cavity and relatively near the mean impingement point (i.e., MIP at $X_{\text{mip}} = 15.05$ cm). As observed from the continuously captured images, the free surface profile varies drastically and fluctuates prominently around the instantaneous impingement point. With reference to Figure 11e,f, Figure 11g shows more decrease of $G_{\text{min}1}$ for the first water–air interface and increasing range of the depth interval ΔY for decrease of the gray level between full air phase (with $G_{\text{max}1} = 255$) and full water phase (with $G_{\text{max}2} = 255$). On the other hand, increase of $G_{\text{min}1}$ is seen clearly in Figure 11g–h. Further, as evidenced in Figure 11f–h, the thickness within which the gray level equals $G_{\text{max}2}$ (representing full water stream from the sliding jet), $(\Delta Y)_{G_{\text{max}2}}$, becomes smaller with an increasing X . It is also found in Figure 11f–h that the representative positions for the local minimum gray level (marked by $G_{\text{min}4}$), $Y_{G_{\text{min}4}}$, lower evidently with increasing streamwise distance. The values of $Y_{G_{\text{min}4}}$ at different sections exactly represent the locations where air bubbles take place most frequently downstream the wedged tip of air cavity.

Figure 12 illustrates the spatial variation of the EAGLD using a total of 9000 images for $10.8 \text{ cm} \leq X \leq 17.5 \text{ cm}$. As elucidated above for the three local minima $G_{\text{min}i}$ (with $i = 1-3$) obtained at $X = 11.4$ cm, the characteristic positions of the three (from first to third) water–air interfaces are identified to be $Y = 3.56, 1.90,$ and 1.11 cm, respectively. In a similar way, the characteristic positions for the three water–air interfaces at different sections can thus be determined. Due to accurate determination of these points, all the points along these interfaces inevitably show certain degree of tiny fluctuations. A moving average technique is thus adopted to smooth these representative interfaces.

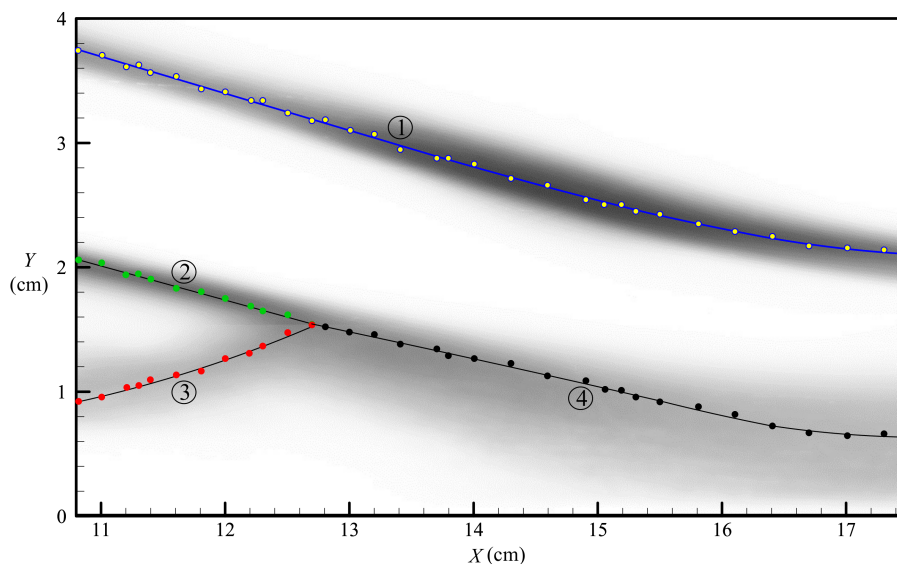


Figure 12. Spatial variation of the ensemble-averaged gray level distribution using 9000 SIM images, together with display of the three water–air interfaces (marked with ①–③) and the virtual boundary (labeled with ④).

Accordingly, the characteristic position for the first minimum value $G_{\text{min}1}$ (marked with ① in Figure 12), $Y = Y_{100\%, \text{wai}}$, denotes statistically the mean one where the first water–air interface appears with a probability of 100%. This fact can be easily reconfirmed by examining these characteristic positions fully occupied by water stream, as seen in the time series of the SIM images captured continuously. Next, the counterpart for the second minimum value $G_{\text{min}2}$ (② in Figure 12) identifies the mean one at which the second water–air interface between the lower free surface of free jet and the upper boundary of air cavity takes place with a probability of about 100%. Similarly, the representative position for the third minimum value $G_{\text{min}3}$ (③ in Figure 12) indicates the mean one, where the third interface exists between the lower boundary of air cavity or the (upper) surface of the recirculation flow, happens with a probability of about 100%. Finally, a virtual boundary (④ in Figure 12), which

consists of the positions having the relatively minimum gray-levels $G_{\min 4}$, stands for the ones where air bubbles pass by most frequently. The streamwise descending of this virtual boundary reveals the trend of the downward motion of air bubbles shed from the wedged tip of air cavity and transported to further downstream at $X = 17.5$ cm.

Furthermore, it would be interesting to summarize the feature of EAGLD near the highly fluctuating free surface of (free or sliding) jet. As seen in Figures 11a–h and 12, a very uniform distribution having a gray level of $G_{\max 1} = 255/G_{\max 2} = 255$ appears over/beneath the upper/lower gray-level gradient zone with the locally lowest gray-level of $G_{\min 1}$. The upper/lower ‘uniform’ gray level can be interpreted as the representative one for each appearance of air phase from the atmosphere/water phase from the (free or sliding) jet. Therefore, the upper gray-level gradient zone reflects the response of intermittent appearance of air phase from the atmosphere and the water–air interface. On the other hand, the lower counterpart correspondingly reveals the response of sporadic appearance of the water–air interface and water phase from the jet. Note that each appearance of air phase would provide a gray level of $G_{\max 1} = 255$ and each appearance of water phase could also contribute a gray level of $G_{\max 2} = 255$, together with each happening of the first water–air interface having a (mean) gray level of $G_{\min 1}$. Due to intermittent occurrence of these two phases with random phase-switching over/below the first water–air interface, the resulted gray level should take the values of $[m \times G_{\max 1} + (N - m) \times G_{\min 1}]/N$ and $[n \times G_{\max 2} + (N - n) \times G_{\min 1}]/N$ for the upper and lower gray-level gradient zones, respectively. Herein, m and n are the times for intermittent appearance of air/water phase accompanied by $(N - m)$ and $(N - n)$ times for fitful appearance of the first water–air interface for $N = 9000$.

Based on the gray-level gradient feature, the probabilistic means for some characteristic positions near the highly fluctuating free surface can be further identified as follows:

- (1) Full air phase with at least 100% appearance of air from the atmosphere or zero appearance of the first water–air interface;
- (2) Intermittent switching between the air phase and the first water–air interface with 50% appearance of the former accompanied by 50% appearance of the latter;
- (3) Almost 100% appearance of the first water–air interface;
- (4) Intermittent switching between the first water–air interface and the water phase with 50% appearance of the former accompanied by 50% appearance of the latter;
- (5) Almost 100% occurrence of the water phase from the jet.

In the following, the notation, $Y_{k\%, \text{wai}} (= Y_{(100-k)\%, \text{air}})$, will be used to represent the position for $k\%$ intermittent appearance of the first water–air interface, together with $(100 - k)\%$ fitful appearance of the air phase from atmosphere in the upper gray-level gradient zone. In addition, $Y_{s\%, \text{wai}} (= Y_{s\%, \text{water}})$, will be employed to stand for the location for $s\%$ fitful occurrence of the first water–air interface, accompanied by $(100 - s)\%$ intermittent happening of water stream from the jet in the lower gray-level gradient zone.

3.5. BTM for Calculating Velocity Components of Individual Air Bubbles

The BTM is employed to trace the movement and calculate the streamwise and transverse velocity components of each targeted air bubble located within a specified observation zone in the images which were captured by SIM. The details of analysis procedure of this method for the velocity components of air bubbles are stated below.

- (1) Calculate the conversion factor (in terms of cm/pixel) from the identified field of view (FOVS₂) used during the SIM measurements at 7.30 cm wide \times 5.70 cm high under a pixel resolution of 1024 \times 800 pixels. Based on this setting, the conversion factor which in fact stands for the length-to-pixel ratio, L_s , is equal to 0.00713 cm/pixel in this study. To show the images for easy illustration and clear identification of respective air bubble in the following steps, a magnified

field of view of the recorded images having 2.28 cm wide \times 1.71 cm high (corresponding to 320×240 pixels) is used.

- (2) Define the abscissa and ordinate coordinates, x and y (in terms of pixel values), parallel with and normal to the chute surface with the ‘virtual origin’ (0, 0) in the (x, y) coordinates (in terms of pixel value), being located at the lower left corner in the magnified images (see Figure 13a–c). The abscissa x is parallel to the X -axis and the ordinate y is identical to the Y . Note that the virtual origin in the (x, y) coordinates corresponds to the position of $(X_0, Y_0) = (15.75, 0)$ cm in the (X, Y) coordinates. Under such a situation, the coordinates for any point of interest in the images can then be identified as (x, y) and expressed as

$$X = X_0 + x \times L_s \quad (9)$$

$$Y = Y_0 + y \times L_s \quad (10)$$

- (3) Select a series of images (taken at a 3000 Hz sampling rate) to be targeted with coded numbers. The serial numbers marked in the images represent the temporal order of images. Then, set three specified vertical lines, which are positioned downstream of the wedged tip of the air cavity, with two equal spacings in between. For example, as seen in Figure 13a–c, the three vertical lines are located at $x = 859, 880,$ and 900 pixel, respectively, with a spacing of about 20 pixel (equivalent to 0.143 cm) between two neighboring lines.

It is worth mentioning that too low of a value of the spacing in the observations actually results in difficulty while precisely determining the two very short time-intervals for an air-bubble rapidly passing through the first two and the latter two of the three vertical lines, and thus induces considerable measuring error in the velocity calculation. On the contrary, too large of a value of the spacing may lead to missing of the temporal and spatial information of the air-bubble features.

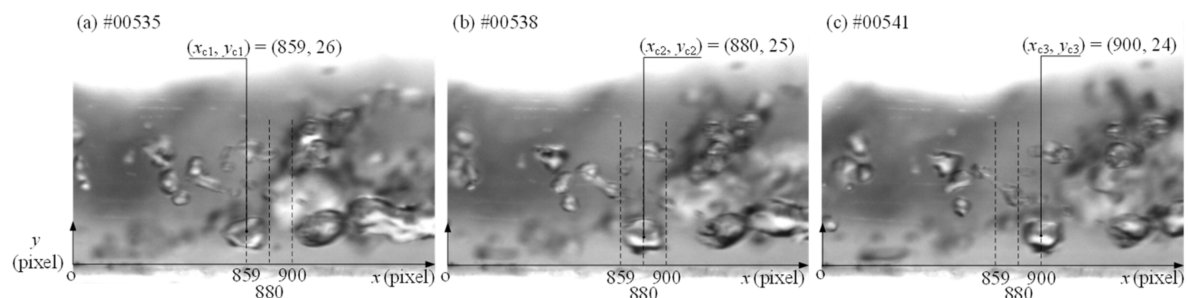


Figure 13. Examples for calculation of the instantaneous streamwise and transverse velocities by using BTM.

- (4) To exactly monitor the centroid of each individual air-bubble exactly passing through the three vertical lines and then find out the image coded numbers and the two corresponding time intervals. Determination of the three coordinates of the centroid of the traced air-bubble was made by visual interpretation along with the aid of software developed by Kashima et al. [31] and Mori et al. [32].

For example, as seen in Figure 13a–c, the coded numbers are #00535, #00538, and #00541, respectively. The three coordinates of the centroid of the traced air bubble on these three lines can be identified in terms of pixel values as: $(x_{c1}, y_{c1}) = (859, 26)$ for Figure 13a, $(x_{c2}, y_{c2}) = (880, 25)$ for Figure 13b, and $(x_{c3}, y_{c3}) = (900, 24)$ for Figure 13c. The time interval between two consecutive numbers is equal to $1/3000$ s, thus the time elapse Δt_1 between Figure 13a,b as well as the counterpart Δt_2 between Figure 13b,c are both equal to $3/3000$ s. The total time interval between Figure 13a,c is therefore equal to $\Delta t = \Delta t_1 + \Delta t_2 = 6/3000$ s.

- (5) Due to the rapid motion of the monitored air bubble, the three coordinates of the centroid of the traced air bubble are sometimes not exactly located on these three original vertical lines and thus biased no more than one pixel upstream or downstream of these three lines. For obtaining the most qualified samples of the traced air bubbles, the positions of the lines are shifted simultaneously one pixel upstream or downstream. Note that simultaneous shifting with one pixel only induces a very small measuring error (corresponding to a tiny displacement of 0.00713 cm and less than 0.7%, to be stated later) in determining the coordinates of the air bubble centroid (see Figure 13a–c).
- (6) Determine the streamwise and transverse velocities, U_b and V_b , of the traced air bubble during the identified time interval Δt as

$$U_b = [(x_{c3} - x_{c1})/\Delta t] \times L_s \quad (11)$$

$$V_b = [(y_{c3} - y_{c1})/\Delta t] \times L_s \quad (12)$$

Note that the calculated velocity just defines the ‘averaged’ one for the targeted air bubble moving from (x_{c1}, y_{c1}) to (x_{c3}, y_{c3}) within the time elapse Δt and with its centroid at (x_{c2}, y_{c2}) on the original or shifted second-line.

For example, the streamwise and transverse velocities of the air bubble with its centroid located at (x_{c2}, y_{c2}) can be obtained as $U_b = 146.2$ cm/s and $V_b = -7.1$ cm/s. It should be mentioned that these two velocity components corresponding to a shift of one pixel downstream for the three vertical lines can be also calculated to be $U_b = 142.6$ cm/s and $V_b = -7.1$ cm/s. The relative error between these two streamwise velocities of the traced air bubble with reference to the approaching velocity at $X = 0$ cm, $U_0 = 214.45$ cm/s, is only 1.68%. This evidence not only demonstrates a very tiny difference between both values and good agreement between both measurement results, but also strongly highlight promising feasibility of the BTM employed in this study.

- (7) Repeat the procedure from step (3) to step (6) for distinct air bubbles passing through the three vertical lines at different heights, and then determine the velocity components of air bubbles.
- (8) Change the images with different serial coded numbers and then repeat the procedure from step (3) through step (7) for calculating the velocity components of air bubbles.

Figure 14a,b presents the distribution of the instantaneous streamwise/transverse velocities (determined by the BTM) and its global trend for over 400 individual air bubbles existing inside the water column for $16.50 \text{ cm} \leq X \leq 17.50 \text{ cm}$ approximately. Note that the increase in the global trend of the instantaneous streamwise velocity distribution along the positive Y direction is clearly witnessed. Meanwhile, scattering of the data point of the instantaneous transverse velocities is seen evidently with wide range of positive and negative values even at a given Y . Due to random motion of each of air bubbles occurring at different heights and times as well as use of the Lagrangian view-point for the BTM, calculation of the mean value at certain Y is thus based on the depth-average of the data within a depth interval of $\Delta Y = 0.1$ cm. These depth-averaged streamwise/transverse velocities of air bubbles, marked by asterisks, are shown in Figure 14a,b.

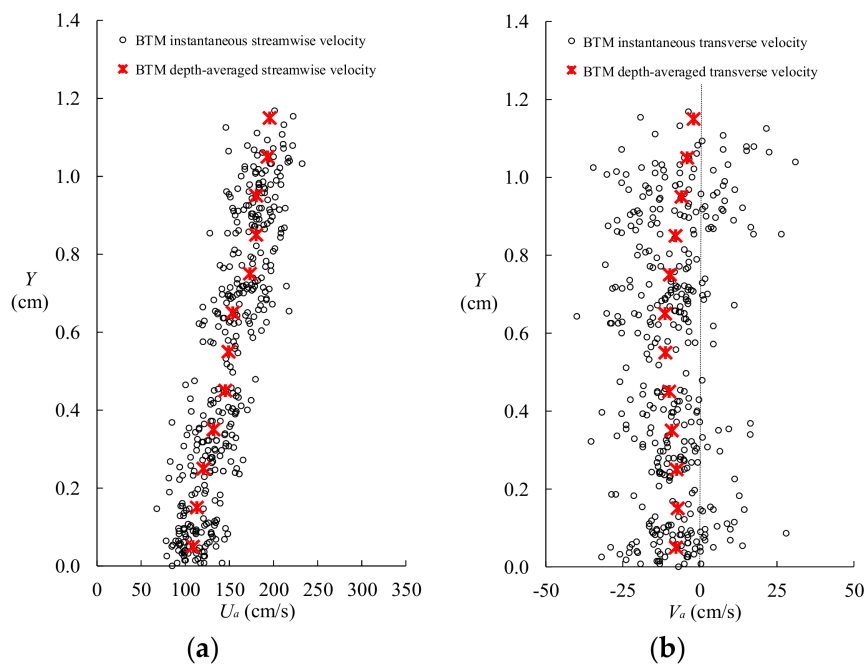


Figure 14. (a,b) The distribution of the instantaneous streamwise/transverse velocity of air bubbles measured by BTM, together with the counterpart of the depth-averaged streamwise/transverse velocity.

3.6. Instantaneous and Mean Velocity Fields Measured by BIV Analysis

The images recorded in the SIM experiments were also used to acquire the velocity field of air bubbles by BIV analysis. Using the cross-correlation technique [42,43], these velocities are calculated from the displacements of the shadows of air-bubble textures (at the pixel points of interest in images) in the X and Y directions. For examples, for $t = 0.02167$, 0.02200 , and 0.02233 s (corresponding to Figure 9n–p), the instantaneous velocity fields of air bubbles are shown in Figure 15a–c. Not only a velocity vector but also a detailed velocity field with distributed vectors are demonstrated even for an individual air bubble. This is because the pixel points on the ‘shadowed’ contour or surface of each air bubble are subjected to continuous deformation, together with the temporal change of shadows. Application of this feature can calculate the velocities at the pixel points and further obtain the velocity field on the occupied region of each air bubble. As illustrated in Figure 9n–p, the detailed 2D movement of each air bubble can be ‘visually sensed’ directly between two neighboring images (only with a time interval of $\Delta t = 1/3000$ s). Therefore, comparisons of the velocities for these specified pixel points which are determined using the BTM (i.e., justified from rapid frame-by-frame display of the continuously recorded images) with those measured with BIV can be further made.

For illustration, only the magnified views for movements of the specified pixel points, say p_1 – p_5 (located on five identifiable locations with prominent shadows), and for the instantaneous velocity field of the air bubble area A (see Figure 9n–p) are shown in Figure 16a,b for $t = 0.02200$ and 0.02233 s. The instantaneous velocity at t is defined as the ratio of the displacement between t and $(t - \Delta t)$ to Δt , with $\Delta t = 1/3000$ s. As shown in the sub-tables of Figure 16a,b, the instantaneous streamwise velocities determined at p_1 – p_5 by BTM agreement with those measured by BIV. The relative errors shown in both sub-tables are less than 2.85% and 2.24%, thus preliminarily confirming the validity of velocity measurements by BIV. Note that the temporal variation in the velocity field of air bubbles varies drastically, with velocity vectors exhibiting fairly distinct magnitudes and different directions even just during a very short time interval of $1/3000$ s. This fact highlights both prominent deformation and rapid movement of the air bubble area A.

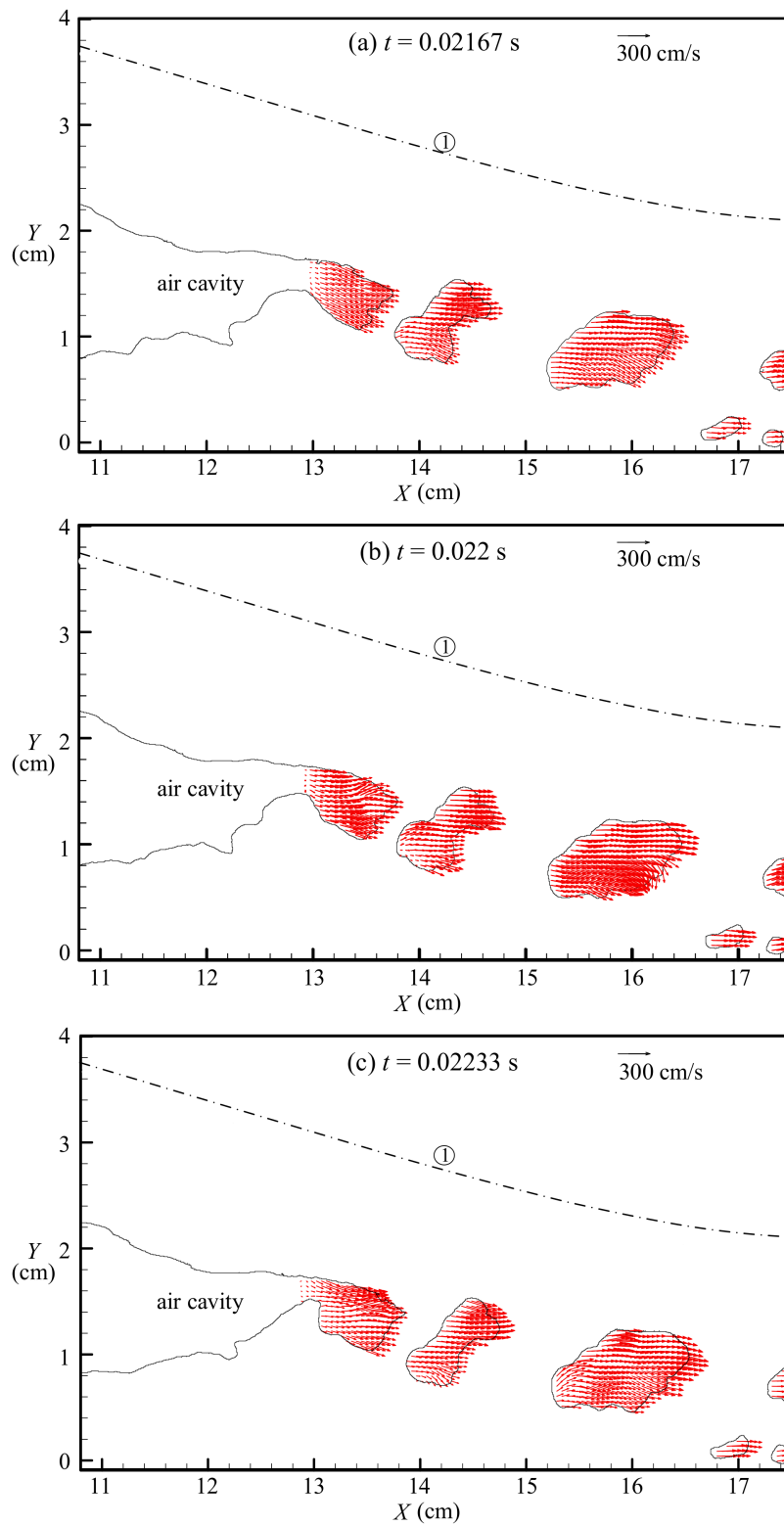


Figure 15. Instantaneous velocity fields of air bubbles at (a) $t = 0.02167$ s; (b) $t = 0.02200$ s; (c) $t = 0.02233$ s using the BIV analysis, along with highlight of the first water–air interface (labeled with ①).

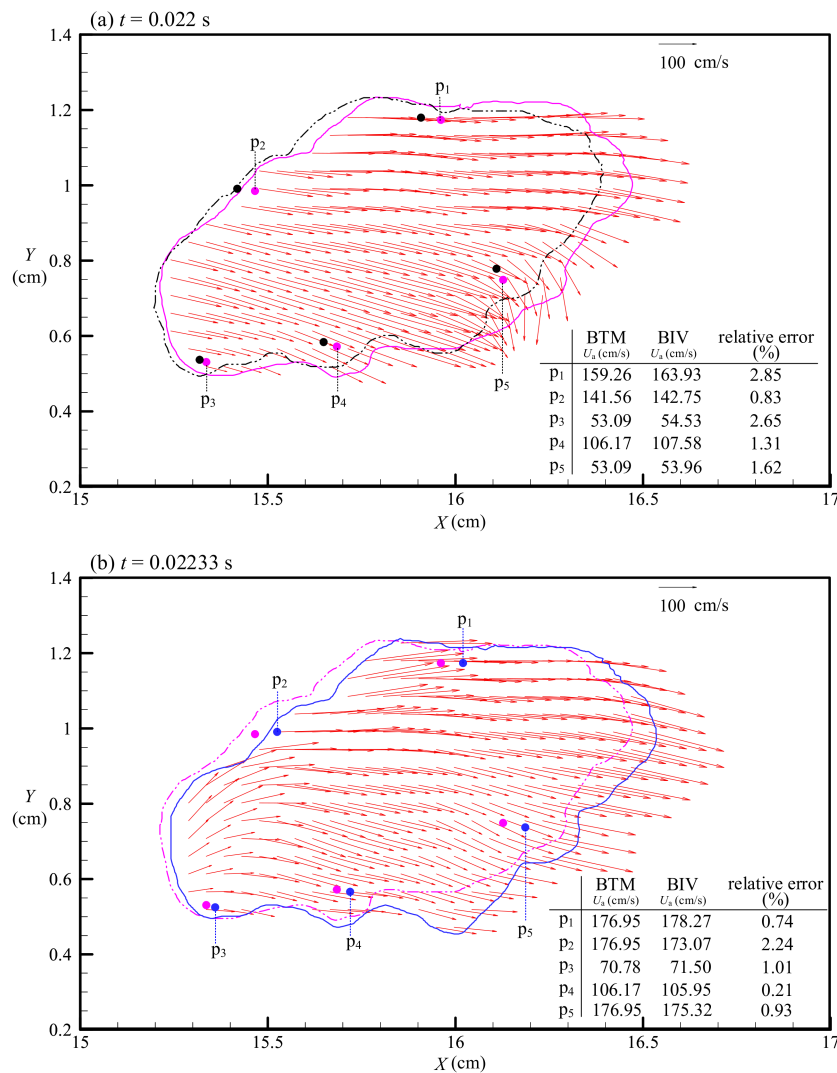


Figure 16. Two magnified views for the instantaneous velocity field of air bubbles A measured by BTM and BIV at (a) $t = 0.02200$ s; (b) $t = 0.02233$ s.

Furthermore, based on the time series of both the visualized images and the instantaneous velocity fields of air bubbles (e.g., Figures 9a–r, 15a–c and 16a,b), it is also recognized that the air-bubble phase consisting of air bubbles occupies the pixel points in the flow domain sporadically (i.e., while in the absence of air-bubble phase, the counterparts are occupied fitfully by the water phase comprising the water stream of the jet). Note that the ‘air-bubble phase’ is particularly used to identify ‘appearance of air bubbles’, but not ‘appearance of air’ from the atmosphere or the air cavity for the air phase. Accordingly, using the phase identification technique (Lindken and Merzkirch [56]; Shi et al. [57]; Adrain and Westerweel [58]; Lee et al. [59]), the probability for air-bubble phase occurring at a specified pixel point of interest can be determined from the time ratio of the shadows (with relatively low gray-levels) of air bubbles appearing intermittently at the pixel point. Figure 17 illustrates the spatial variation of the probability for intermittent occurrence of air-bubble phase within the flow domain for a total of 27,000 images. The three characteristic interfaces (marked with ①–③) in Figure 12 are also plotted in Figure 17, together with display of the virtual boundary (④). The trend of the positions for the local maximum probability of intermittent appearance of the air-bubble phase fairly matches the virtual boundary, which highlights the locations for the most frequent occurrence of air bubbles.

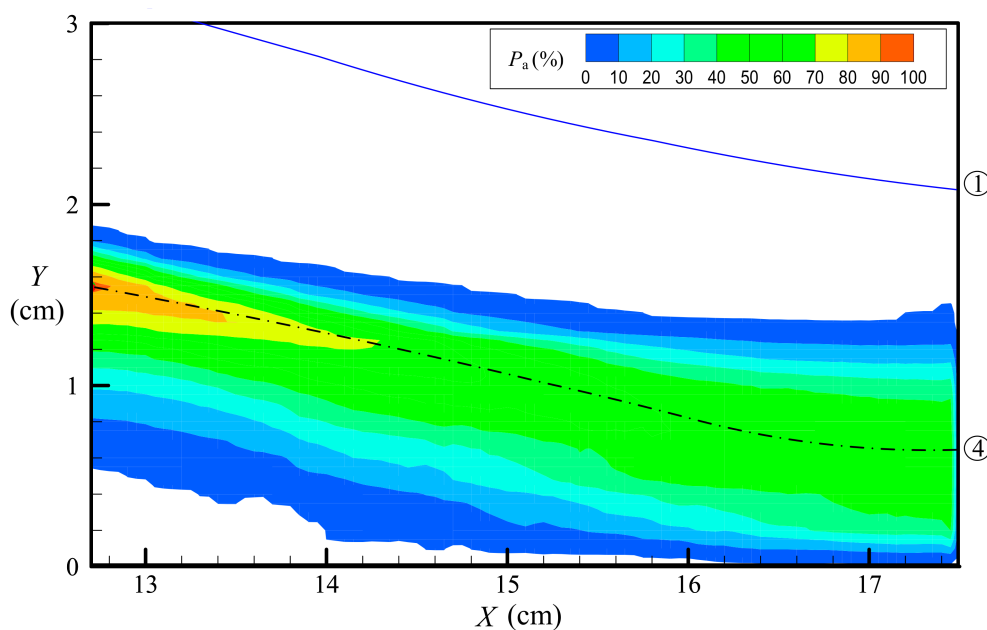


Figure 17. Spatial variation of the probability for intermittent occurrence of air bubbles, along with exhibition of the first water–air interface (labeled with ①) and the virtual boundary (④).

Moreover, the probability distribution of air-bubble phase at $X = 17.0$ cm is extracted from Figure 17 and then illustrated in Figure 18a. The probability increases from 0 at $Y = 0$ cm (the chute surface) to a maximum of 47.74% at $Y = 0.65$ cm, where air bubbles appear most frequently thus corresponding to the lowest ensemble-averaged gray level. Then it decreases from the maximum to zero at $Y = 1.4$ cm, over which no air bubble exists in the water stream of jet. Because evident downward motion of air bubbles prevails while they are transported from the wedged tip of air cavity to the downstream section at $X = 17.0$ cm. Accordingly, Figure 18b,c presents the overall time-averaged streamwise/transverse velocities of air bubbles along Y , obtained by multiplying the depth-averaged streamwise/transverse velocities (see Figure 14a,b) with the corresponding probabilities (Figure 18a). The overall time-averaged (streamwise/transverse) velocity is hereafter called mean (streamwise/transverse) velocity for brevity.

Figure 18b,c illustrates comparison of the profile of the mean streamwise/transverse velocity of air bubbles for $X = 17.0$ cm determined by BIV analysis with the counterpart obtained by BTM for FOVS₂. Not only the nature of variation but also the velocity magnitudes obtained by the former method are in good agreement with those acquired by the latter, strongly indicating validity of the velocity determination by the BIV analysis. The maximum value of mean streamwise velocity occurs at around $Y = 0.85$ – 0.90 cm (Figure 17b), but not at $Y = 0.65$ cm (where the maximum probability of intermittent appearance of air bubbles occurs), due to an increasing trend of the depth-averaged streamwise velocity distribution of air bubbles. However, the negative maximum of the mean transverse velocity appears at about $Y = 0.65$ cm (see Figure 18c), highlighting each contribution of downward motion of air bubbles taking place most frequently herein.

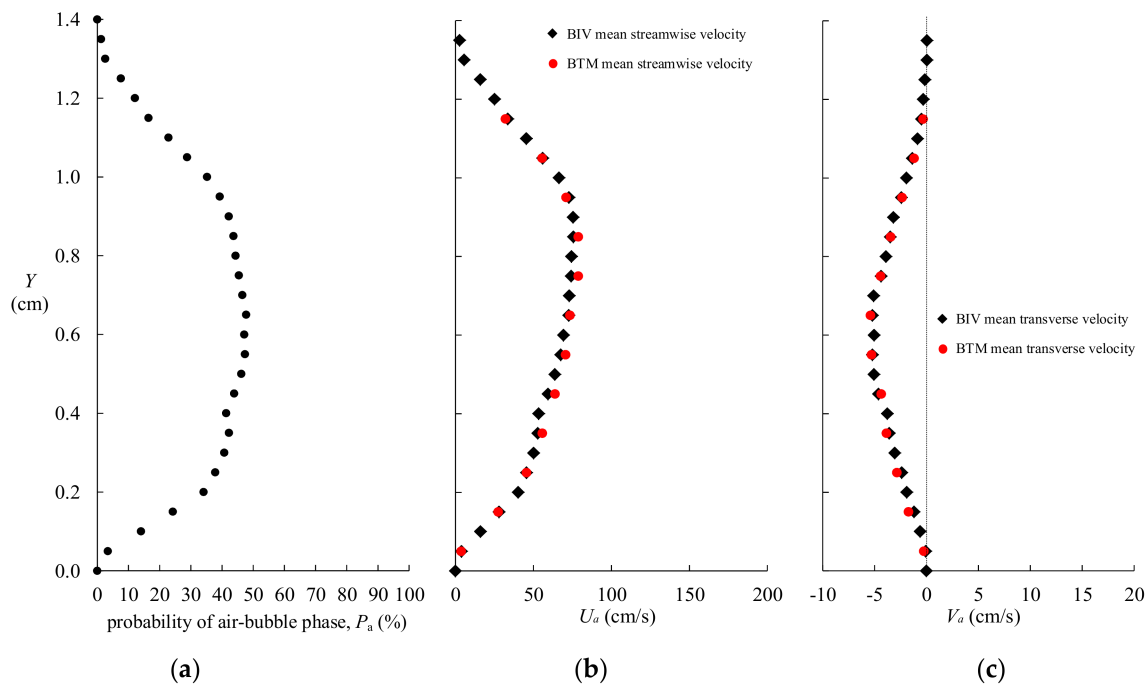


Figure 18. (a) Probability distribution for intermittent occurrence of air bubbles at $X = 17.0$ cm; (b,c) comparison of the mean streamwise/transverse velocity profile of air bubbles determined by BTM with that obtained by BIV analysis.

The mean velocity field of air bubbles for $12.7 \text{ cm} \leq X \leq 17.5 \text{ cm}$ is shown in Figure 19a, in which the first water–air interface (marked with ①) and the virtual boundary (④) are both plotted. For the velocity profile at a specified section, the mean velocity increases from 0 (in the relatively lower portion) to a local maximum (taking place somewhat beyond the virtual boundary), then decreases to 0 (in the relatively higher portion). Furthermore, the distribution range between these two zero velocity in the Y direction increases with an increasing X . For visual aid, a dashed line (⑤) is plotted to highlight the locations for occurrence of the local maximum mean velocity, indicating that these positions are all higher than those on the virtual boundary. The reason can be again attributable to the fact that either the global trend of the instantaneous streamwise velocities or the depth-averaged streamwise velocity of air bubbles does increase with an increasing Y , as stated above for Figure 14a,b. Due to the prominent downward motion of air bubbles prevailing in the flow field for $12.7 \text{ cm} \leq X < 18.5 \text{ cm}$, no air bubble exists between the free surface of the jet and the zero-velocity position located in the relatively higher portion. Instead, the full water phase of the jet dominates this zone.

Figure 19b presents variations of the maximum magnitudes of mean streamwise and transverse velocities of air bubbles, $(U_a)_{\max}$ and $(V_a)_{\max}$. As seen in Figure 19b, $(U_a)_{\max}$ increases a little from 96.1 cm/s at $X = 12.7$ cm to the peak value of 104.2 cm/s at $X = 13.7$ cm, then keeps decreasing down to 73.0 cm/s at $X = 16.25$ cm, and again increases slightly to 76.4 cm/s at $X = 17.3$ cm. On the other hand, the magnitude of $(V_a)_{\max}$ increases from 18.3 cm/s at $X = 12.7$ cm to the maximum value of 22.84 cm/s at $X = 13.7$ cm, then starts decreasing monotonically to around 3.0 cm/s at $X = 17.15$ – 17.3 cm. Due to the magnitudes of $(U_a)_{\max}$ far larger than those of $(V_a)_{\max}$, nature of variation in the resultant maximum mean velocity of air bubbles, $[V_a]_{\max} (= \{[(U_a)_{\max}]^2 + [(V_a)_{\max}]^2\}^{1/2})$ almost follows that of the $(U_a)_{\max}$.

It is worth mentioning that, similar to calculation for the water stream, the integral time scales of the streamwise and transverse fluctuating velocities of air-bubbles $u_a(t)$ and $v_a(t)$, obtained at $(X, Y) = (15.05, 1.10)$ cm, are estimated to be $T_{its,u_a} = 0.00135$ s and $T_{its,v_a} = 0.00120$ s, demonstrating their very small values. For each run, the corresponding sampling duration is $T_{sd,a} = 3.0 \text{ s} = 2222 \times T_{its,u_a} = 2500 \times T_{its,v_a}$. Three repeated runs were performed for the BIV analysis with a total sampling

duration of $3T_{sd,a} = 9.0 \text{ s} = 6666T_{its,u_a} = 7500T_{its,v_a}$ [i.e., with a total of $(3 \times 3 \times 3000)$ samples] in the present study. From the preliminary test, the mean velocities of air bubbles obtained using 18,000 samples are nearly identical to $U_a = 87.1 \text{ cm/s}$ and $V_a = -16.8 \text{ cm/s}$ for using 27,000 samples (both with the relative error being less than 1.5%), confirming convergence of the data employed. Therefore, the mean velocity characteristics of air bubbles stated above can be assured due to the total sampling duration $3T_{sd,a}$ being extremely larger than T_{its,u_a} and T_{its,v_a} .

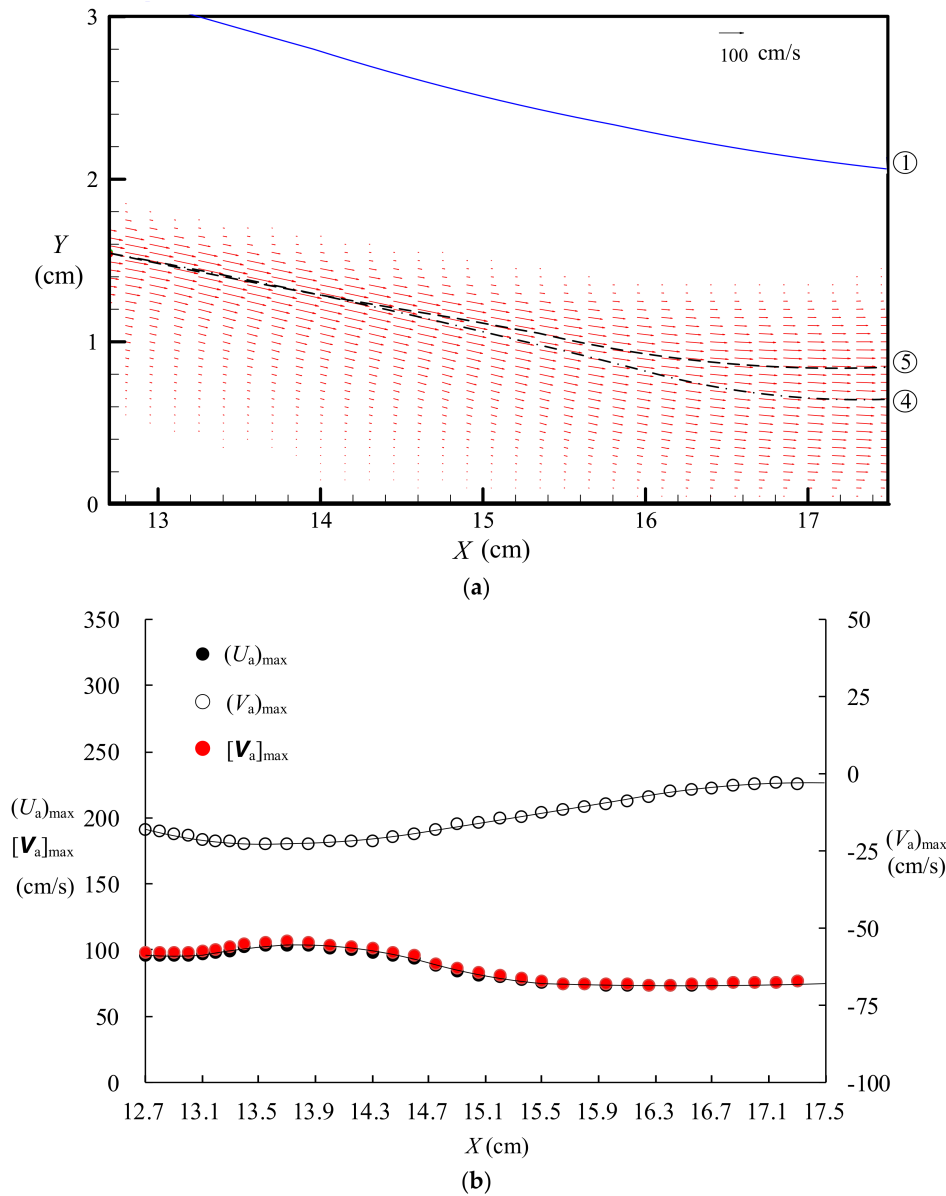


Figure 19. (a) Mean velocity field of air bubbles for $12.7 \text{ cm} \leq X \leq 17.5 \text{ cm}$, in which the first water–air interface (marked by ①), the virtual boundary (④), and the dashed curve representing positions for the maximum mean streamwise velocity (⑤) are highlighted; (b) Variations of the maximum mean streamwise, transverse, and resultant velocities of air bubbles, i.e., $(U_a)_{\max}$, $(V_a)_{\max}$, and $[V_a]_{\max}$.

3.7. Construction of Two-Phase Velocity Field

Using the mean velocity field measured by HSPIV and the counterpart obtained by BIV for 27,000 images, construction of the two-phase mean velocity field can be realized by merging these two together. Figure 20 presents the two-phase velocity field for $12.7 \text{ cm} \leq X \leq 17.5 \text{ cm}$, with the

water phase/air-bubble phase velocity vectors marked by black and red arrows. Several flow features underlying Figure 20 are addressed as follows:

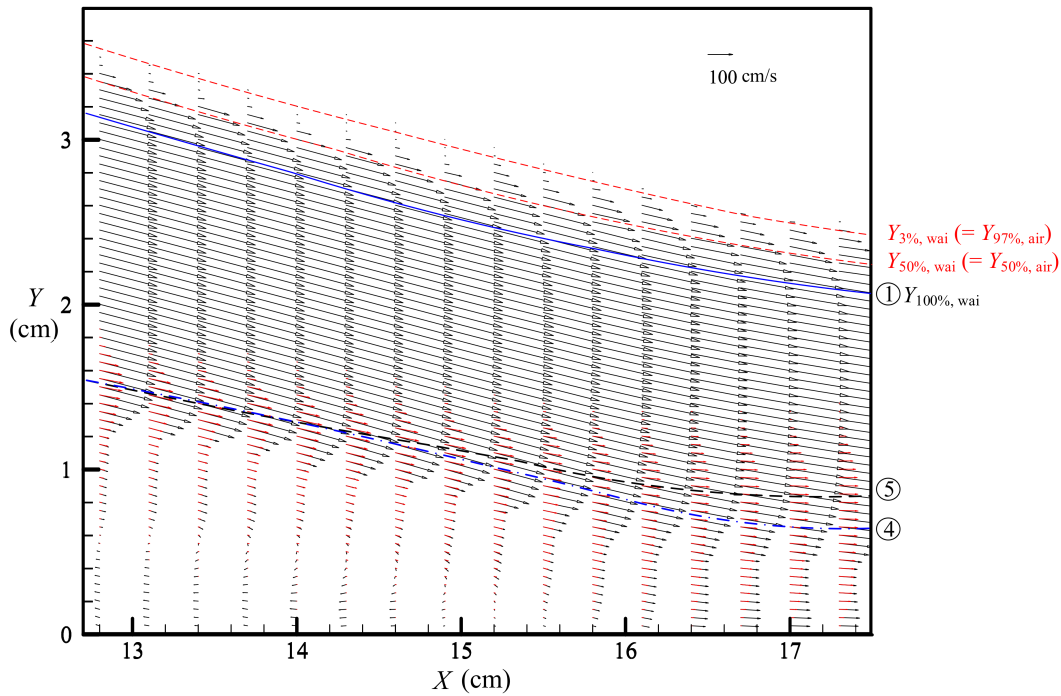


Figure 20. Two-phase velocity field consisting of the water phase/air-bubble phase velocity vectors marked by black/red arrows.

Firstly, for the water stream right beneath the free surface, each mean velocity distribution exhibits a relatively uniform profile and holds locally a characteristic uniform velocity of $[V_w]_u (= [(U_{wu})^2 + (V_{wu})^2]^{1/2})$ at each section. For example, at $X = 12.8$ cm, $U_{wu} = 230.9$ cm/s and $V_{wu} = -60.1$ cm/s, thus leading to $[V_w]_u = 238.6$ cm/s. In addition, at $X = 16.4$ cm, $U_{wu} = 215.7$ cm/s and $V_{wu} = -41.3$ cm/s, resulting in $[V_w]_u = 219.6$ cm/s. These two examples indicate that the local uniform streamwise velocity, U_{wu} , is far larger than the magnitude of the local uniform transverse velocity, V_{wu} . Moreover, for the velocity distribution in the highly fluctuating free surface zone, the non-uniform feature with prominent velocity gradient is clearly evidenced. Herein, for clear identification, $Y_{3%, wai}$, instead of $Y_{1%, wai}$, is designated equivalently as the position at which almost full air phase occurs.

Secondly, a characteristic position of $Y_{50%, wai} (= Y_{50%, air})$, located within the highly fluctuating free surface zone between $Y_{100%, wai}$ and $Y_{3%, wai}$, is used to characterize the one for intermittent switching of the water–air interface with 50% appearance, which is accompanied by 50% appearance of air phase from the atmosphere. Since the profile of EAGLD at a specified section $G(Y)$ and its corresponding regression form can be obtained from Figure 11, it is thus easy to acquire the first derivative of the fitted gray level with respect to Y (i.e., the slope of the gray level), $\partial G/\partial Y$. For example, the plot of $\partial G(Y)/\partial Y$ at $X = 13.4$ cm is presented in the left panel of Figure 21a. The maximum value of $\partial G/\partial Y$ is found to take place at the specified height where the inflection point is located, i.e., $Y_{in, gl}$. Furthermore, the gray-level at the inflection point is examined to be $[G_{min1} + G_{air}]/2 = (93 + 255)/2 = 174$, exactly equivalent to the ‘half-width’ feature of the gray-level distribution within the highly fluctuating free surface, i.e., $Y_{in, gl} = Y_{hw, gl} = 3.192$ cm. Meanwhile, the right panel of Figure 21a illustrates the mean streamwise velocity distribution of water stream $U_w(Y)$ and its first derivative $\partial U_w(Y)/\partial Y$ at the same section, exhibiting that the inflection point and half-width position (where the fitted velocity is exactly equal to $U_{wu}/2$) in the ‘velocity profile’ are identically located at $Y = Y_{in, vp} = Y_{hw, vp} = 3.197$ cm. After further detailed comparison for other sections at $X = 15.05$ and 17.00 cm

(Figure 21b,c), all of these characteristic positions are found to be almost identical and nearly equal to $Y_{50\%, wai}$. Namely, $Y_{in, gl} = Y_{hw, gl} = Y_{in, vp} = Y_{hw, vp}$.

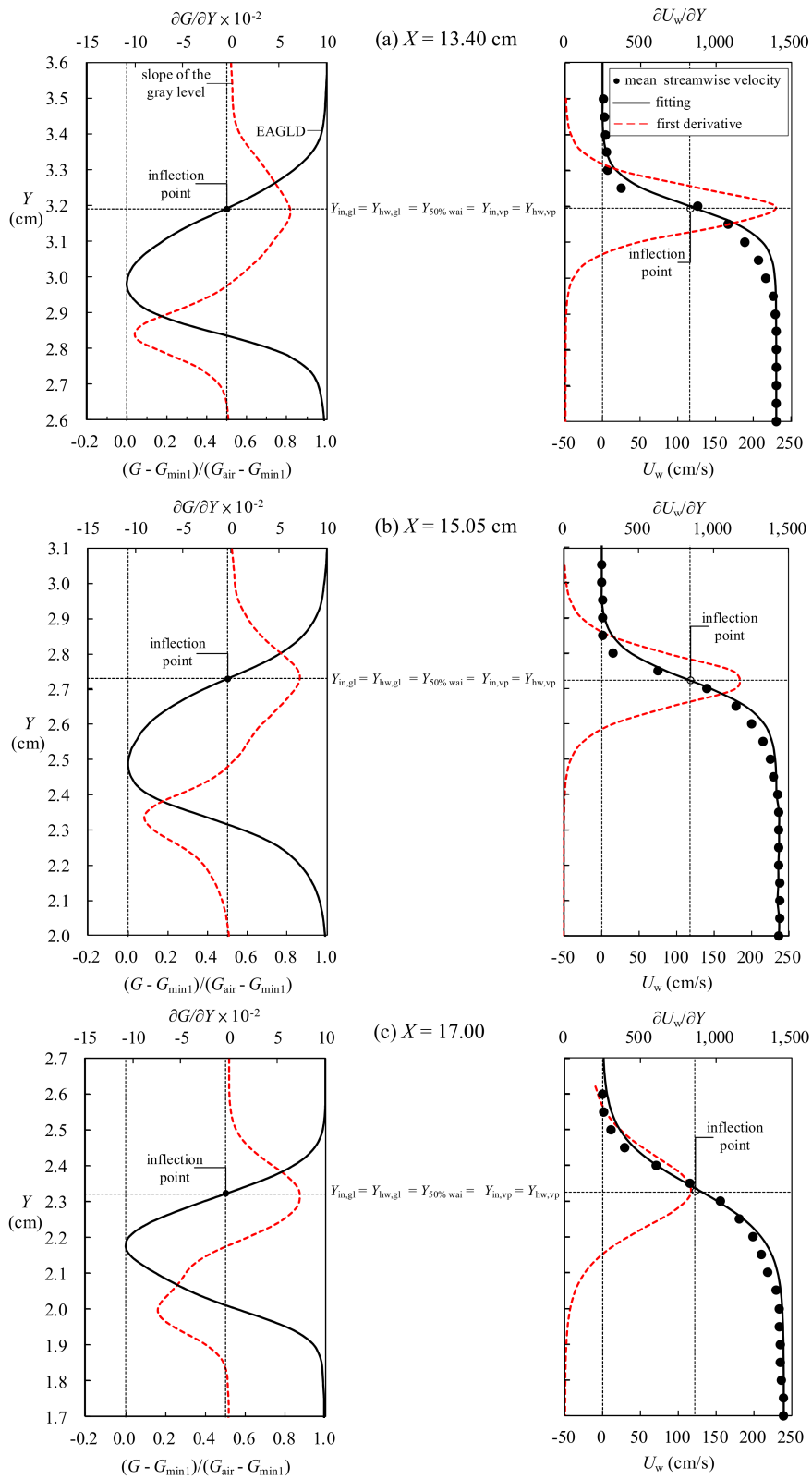


Figure 21. Plots of both $G(Y)$ and $\partial G(Y)/\partial Y$ shown in the left panel as well as both $U_w(Y)$ and $\partial U_w(Y)/\partial Y$ in the right panel for (a) $X = 13.40$ cm; (b) $X = 15.05$ cm; (c) $X = 17.00$ cm.

Thirdly, a relatively large size of recirculation flow beneath the virtual boundary is distinctly observed for the water phase, with the mean impingement point (MIP) located at $X = X_{\text{mip}} = 15.05$ cm. As evidenced from the continuous SIM images, flow bifurcation over the chute surface takes place in the vicinity of the MIP, upon which the ‘water stream’ of the sliding jet impinges frequently. However, most of air bubbles entrained downward in the sliding jet impinge the chute surface further downstream the MIP due to their smaller downward velocities (as shown in Figure 19b and further demonstrated in Figure 22). Therefore, the mean situation of flow bifurcation can be characterized by the slowly reversed water-stream moving upstream from the MIP section, the zero-velocity occurring right at the MIP section, and the relatively rapid water-stream transporting downstream from the MIP section. On the other hand, flow bifurcation hardly occurs for the air phase.

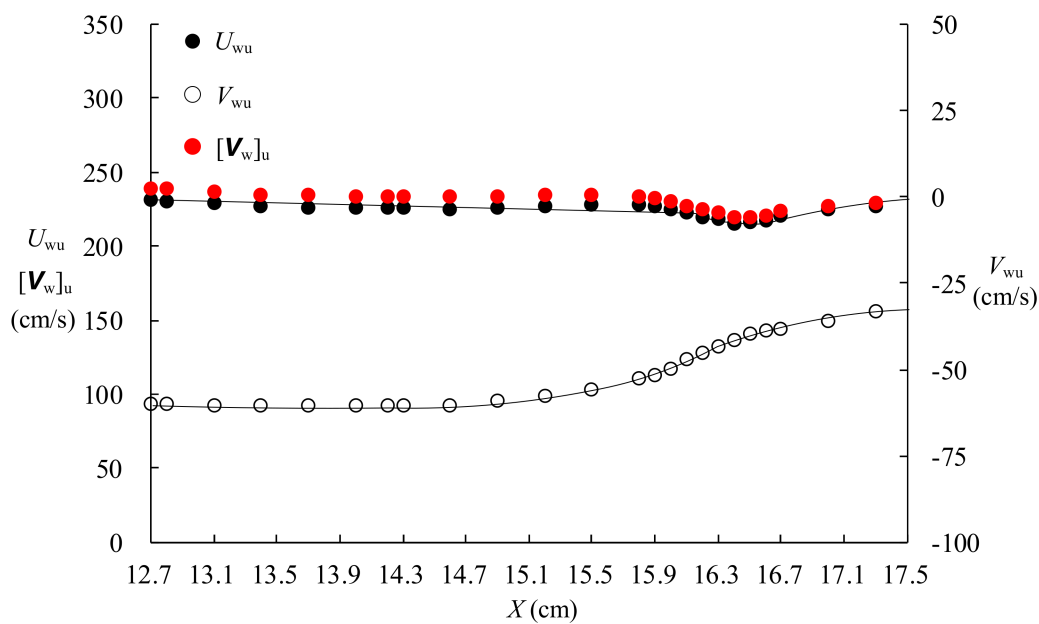


Figure 22. Variations of U_{wu} , V_{wu} and $[V_w]_u$ against X .

Fourthly, as mentioned above in Figure 19b, the streamwise distribution of the locally maximum value of mean streamwise velocity of air bubbles has been addressed, with its magnitude varying from 96.1 cm/s at $X = X_{\text{mip}} = 12.7$ cm to the peak value of 104.2 cm/s at $X = 13.7$ cm, then down to 73.0–76.4 cm/s at $X = 16.25$ – 17.3 cm. Figure 22 illustrates the variations of the uniform streamwise and transverse velocities of water stream, U_{wu} and V_{wu} . As shown in Figure 22, the variation of U_{wu} exhibits roughly a linear decreasing trend from 231.5 cm/s at $X = 12.7$ to 227.9 cm/s at $X = 15.8$ cm, then U_{wu} decreases more prominently to 215.7 cm/s at $X = 16.4$ cm, and again increases slightly to 226.7 cm/s at $X = 17.3$ cm. Furthermore, the V_{wu} magnitude increases somewhat from 59.6 cm/s at $X_{\text{mip}} = 12.7$ cm to 60.5 cm/s at $X = 14.2$ cm, then keeps decreasing to 33.3 cm/s at $X = 17.3$ cm. It is thus realized that the magnitudes of the mean streamwise velocities for air bubbles are all smaller than those of the uniform streamwise velocity for water stream, with the former being only 0.33–0.5 times the latter. For $12.7 \text{ cm} \leq X < 17.5 \text{ cm}$, the ratio of the maximum streamwise velocity of air bubbles to the uniform streamwise velocity of water stream, $(U_a)_{\text{max}}/U_{wu}$, is demonstrated in Figure 23, in which the range of this ratio, $(U_a)_{\text{max}}/U_{wu}$, varies between 0.32 and 0.44 with an average of 0.38. As reported in Lin et al. [35] for the steady hydraulic jumps downstream of a sluice gate (with $F_{r0} = 4.51$ – 5.35), the corresponding ratio of the maximum horizontal air-bubble velocity to the maximum horizontal water velocity was between 0.6 and 0.8 with an averaged ratio of 0.67. Therefore, the values for the range and the average of this ratio for the present two-phase chute flow (with $F_{r0} = 4.23$ at $X = 0$ cm) are both smaller than those for the steady hydraulic jumps.

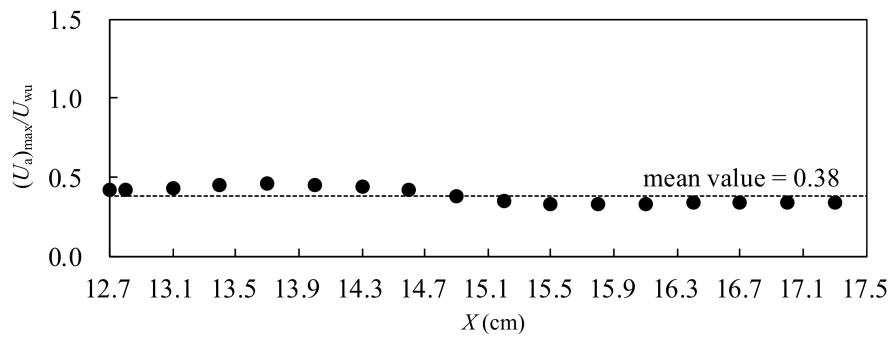


Figure 23. Variation of $(U_a)_{\max}/U_{wu}$ with X .

Fifthly, for further insight into the features of the two-phase velocity field, the profiles of the streamwise and transverse velocities for both water and air-bubble phases, together with the probability distribution of the air bubble phase at three distinct sections are illustrated in Figures 24a–c, 25a–c and 26a–c. For $X = 13.4$ cm in Figure 24a–c (i.e., slightly downstream of $X_{mwt} = 12.7$ cm), the maxima of the mean streamwise and transverse air-bubble velocities both take place right at the characteristic point for the maximum probability of air-bubble phase, $Y = 1.40$ cm. These two positions are also situated at the juncture between the uniform velocity zone and the velocity gradient zone in the mean water velocity profiles, highlighting the shearing effect on the entrainment of air bubbles (Rutschmann [11]). The features for the counterparts obtained at $X = 14.3$ cm are identical to those for $X = 13.4$ cm (not shown).

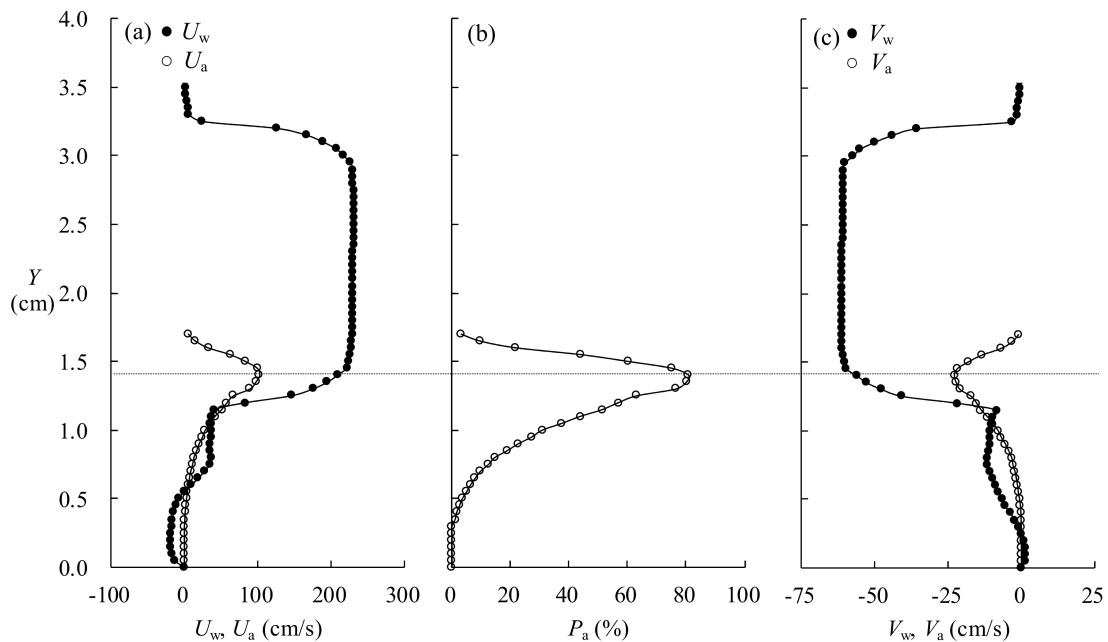


Figure 24. Relationship among (a) the profiles of mean streamwise velocities of both water stream and air-bubble phases; (b) the probability distribution for intermittent occurrence of air bubbles, and (c) the profiles of mean transverse velocities of both phases at $X = 13.4$ cm.

Figure 25a–c shows the counterpart for $X_{mip} = 15.05$ cm (i.e., at the MIP section), the maxima of the mean streamwise and transverse air-bubble velocities both occur also at the characteristic point for the maximum probability of air-bubble phase, $Y = 1.0$ cm. However, the two specified positions are within the velocity gradient zones of the mean streamwise and transverse water velocity profiles, revealing the relative lowering of the specified positions and the prevailing of the downward motion of air bubbles. For $X = 15.8$ cm (i.e., slightly downstream of $X_{mip} = 15.05$ cm, not shown), the maxima of the

mean streamwise and transverse air-bubble velocities both appear at $Y = 1.0$ cm, higher than $Y = 0.75$ cm at which the maximum probability of air-bubble phase occurs. Nevertheless, these characteristic points are situated completely inside the velocity gradient zone of the mean water velocity profiles. This witness reveals clearly obvious thickening of the gradient zones of the water-phase velocity profiles near the MIP section, again confirming the downward motion of air bubbles. Such a flow feature still holds and becomes more prominent at a section further downstream, as evidenced in Figure 26a–c for $X = 17.0$ cm.

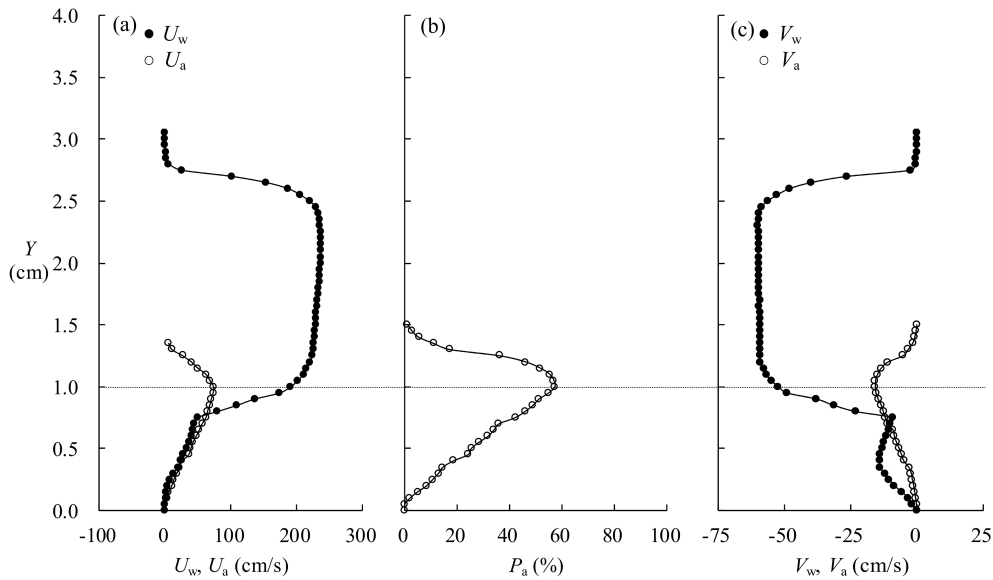


Figure 25. Relationship among (a) the profiles of mean streamwise velocities of both water stream and air-bubble phases, (b) the probability distribution for intermittent occurrence of air bubbles, and (c) the profiles of mean transverse velocities of both phases at $X = 15.05$ cm.

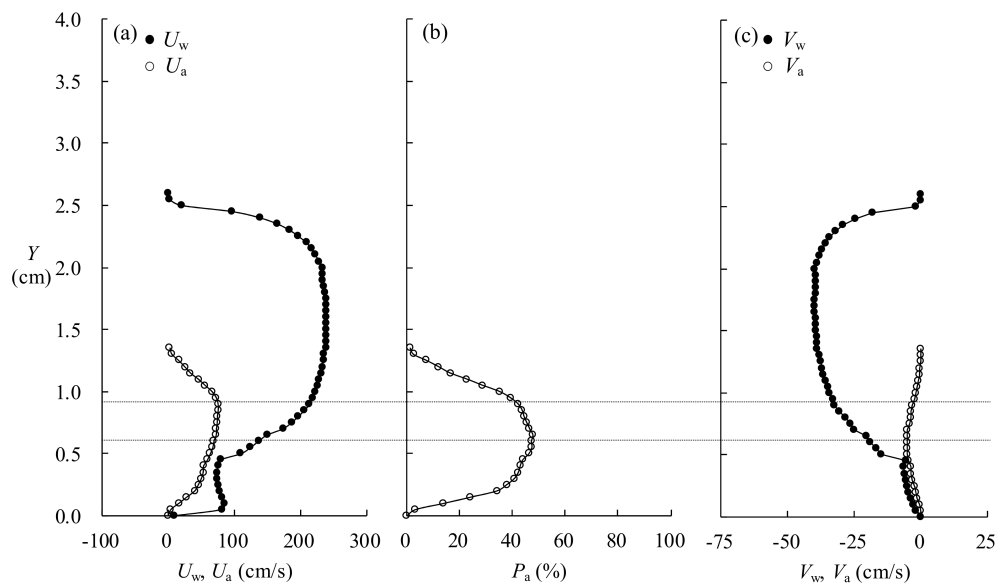


Figure 26. Relationship among (a) the profiles of mean streamwise velocities of both water stream and air-bubble phases, (b) the probability distribution for intermittent occurrence of air bubbles, and (c) the profiles of mean transverse velocities of both phases at $X = 17.0$ cm.

4. Conclusions

In the two-phase flow of a chute aerator formed by an offset, four different image-based techniques—i.e., SIM, HSPIV, BTM, and BIV—have been utilized to display three water–air interfaces and the virtual boundary, to determine profiles of the instantaneous and mean streamwise and transverse velocities of air bubbles, to predict the probability distribution for intermittent occurrence of air bubbles; and to obtain the mean velocity fields of water stream and air bubbles. A target experiment with an approach water depth of 2.62 cm and a Froude number of 4.23 at the offset is performed. The measurement and observation region is deployed from the upstream neighborhood of the wedged tip of air cavity to further downstream of flow impingement point, within which air bubbles are released and then entrained into a water stream with prominent downward motion. Based on the visualized images and measured results, the findings are summarized as follows:

1. The non-fully developed approach flow condition for the present aerated chute flow and the fully developed counterpart for the free overfall over a vertical drop (Rajaratnam and Chamani [51]) both witness the fairly uniform velocity distribution of the free jet, strongly highlighting its independence of these two distinct approach flow conditions.
2. Successful removal of the noise-like blurred background and foreground located outside of the DOF in the SIM images not only warrants clear identification of three water–air interfaces and movements of discrete air bubbles in the instantaneous images, but also provides convincing measurement results of the instantaneous and mean air-bubble velocity profiles/fields using the BTM and BIV analysis.
3. Air bubbles are produced and then shed mainly by one of the following three ways: (1) From a whole wedged tip of air cavity without branching; (2) from different finger-like branches at the wedged tip of air cavity; (3) from the formation of relatively convergent wedge-shaped tip from which the air bubbles are generated directly. For the present target experiment, the averaged time duration for the shedding process of air bubbles is estimated to be 0.0102 s, together with a maximum of 0.0323 s and a minimum of 0.001 s.
4. For $12.7 \text{ cm} \leq X < 18.5 \text{ cm}$, almost all of the air bubbles are transported rapidly downstream by the sliding jet with prominent downward motion. However, for $X > 18.5 \text{ cm}$, the air bubbles still move fast downstream but with evident lifting motion, which is induced by the buoyant force.
5. Near the highly fluctuating free surface of the (free or sliding) jet, a uniform distribution having the maximum gray level of $G_{\max 1} = 255/G_{\max 2} = 255$ appears over/beneath the upper/lower gray-level gradient zone, together with each instance of the first water–air interface having a mean gray level of $G_{\min 1}$. The upper gray-level gradient zone thus reflects the response of intermittent appearance of air phase from the atmosphere or the first water–air interface. Meanwhile, the lower counterpart represents the response of fitful appearance of the first water–air interface or water phase from the jet. Due to intermittent occurrence of these two phases with random phase-switching over/below the first water–air interface, the resulted gray levels take the values of $[m \times G_{\max 1} + (N - m) \times G_{\min 1}]/N$ and $[n \times G_{\max 2} + (N - n) \times G_{\min 1}]/N$ (with $N = 9000$) for the upper and lower gray-level gradient zones, respectively.
6. The characteristic position for the first minimum value $G_{\min 1}$, $Y = Y_{100\%, \text{wai}}$, represents statistically the mean one where the first water–air interface occurs with a probability of 100%. The counterpart for the second minimum value $G_{\min 2}$ justifies the mean one at which the second water–air interface between the lower free surface of free jet and the upper boundary of air cavity appears with a probability of 100%. Furthermore, the representative position for the third minimum value $G_{\min 3}$ identifies the mean one, where the third water–air interface exists between the lower boundary of air cavity or the (upper) surface of the recirculation flow, happens with a probability of 100%. Convergence of the averaged geometric shape of air cavity into a wedged tip takes place at $X_{\text{mwt}} = 12.7 \text{ cm}$, where the second water–air interface merges with the third one. Finally, a virtual boundary, which consists of the positions having the relatively minimum

gray-levels $G_{\min 4}$, stands for the ones where air bubbles pass by most frequently. Streamwise descending of this virtual boundary clearly exhibits the trend of downward motion of air bubbles while they are transported downstream up to $X = 18.5$ cm. However, prominent lifting motion of air bubbles is witnessed for $X > 18.5$ cm.

7. A characteristic position $Y_{50\%, \text{wai}} (= Y_{50\%, \text{air}})$, which is located within the highly fluctuating free surface zone between $Y_{100\%, \text{wai}}$ and $Y_{0\%, \text{wai}} (= Y_{100\%, \text{air}})$, characterizes the intermittent switching of the first water–air interface with 50% appearance, which is accompanied by 50% appearance of air phase from the atmosphere. All of these characteristic positions $Y_{50\%, \text{wai}} (= Y_{50\%, \text{air}})$ are almost identical to the specified heights where the inflection point and half-width of both the ensemble-averaged gray-level distribution and the mean streamwise velocity profiles are located. Namely, $Y_{50\%, \text{wai}} = Y_{\text{in, gl}} = Y_{\text{hw, gl}} = Y_{\text{in, vp}} = Y_{\text{hw, vp}}$.
8. Using the BIV analysis for the SIM images, a very detailed velocity field with many vectors has been displayed for an individual air-bubble contour, over which the BTM is also performed. The nature of variation and velocity magnitudes acquired by the former method at $X = 17.0$ cm are in good agreement with those obtained by the latter, pointing out the validity of velocity determination in the BIV analysis.
9. A relatively large size of recirculation flow beneath the virtual boundary is observed evidently for the water phase, with the MIP located at $X_{\text{mip}} = 15.05$ cm. Such a flow bifurcation can be characterized by the slowly reversed stream moving upstream from the MIP section, the zero velocity right appearing at the MIP section, and the relatively rapid stream moving downstream from the MIP section. On the other hand, no (mean) flow bifurcation occurs for the air-bubble phase.
10. For $12.7 \text{ cm} \leq X \leq 17.5 \text{ cm}$, the maximum value of mean streamwise velocities of air bubbles are all smaller than those of the uniform streamwise velocity of water stream. The ratio of the maximum mean streamwise velocity of air bubbles to the uniform streamwise velocity of water stream, $(U_a)_{\text{max}}/U_{\text{wu}}$, ranges between 0.32 and 0.44 with an average of 0.38, which is less than the counterpart of the steady hydraulic jumps having an averaged ratio of 0.67 (Lin et al. [35]).
11. At the sections located a little downstream of $X_{\text{mwt}} = 12.7$ cm, the maxima of the mean streamwise and transverse velocities of air bubbles both appear not only at the characteristic height for the maximum probability of air-bubble phase; but also at the juncture between the uniform-velocity zone and the velocity-gradient zone in the mean velocity profiles of water stream. This evidence highlights the shearing effect on the entrainment of air bubbles. Nevertheless, for $X \geq X_{\text{mip}} = 15.05$ cm, these two characteristic heights are both situated completely inside the velocity-gradient zone of the mean velocity profiles of water stream. This feature reveals obvious thickening of the velocity-gradient zone in the velocity profile of air bubbles near the MIP section, exhibiting further downward motion of air bubbles.

It is expected that the combination of these four optic-based techniques, together with the frame structure of working items as shown in Figure 3, can be effectively and widely applied to various two-phase flow fields with liquid–air interfaces over the free (or internal) surface and air bubbles in the flow.

Author Contributions: C.L. was responsible for project administration, conceptualization of the research, technical supervision and quality control of experimental results; with participation from J.Y. for partial funding acquisition, project planning, and tests; and from P.T. for assistance with the experiments. Execution of the tests, mathematical formulation of image processing methodology, and data analysis were performed by M.K. The manuscript was written by C.L. Manuscript revisions were modified by R.R. and J.Y. All the authors contributed to its final version.

Funding: The study was carried out as part of a research project “Hydraulic design of chute spillway aerators”, funded by the Swedish Hydropower Centre (SVC). SVC has been established by the Swedish Energy Agency, Energiforsk and Svenska Kraftnät together with Royal Institute of Technology, Luleå University of Technology, Chalmers University of Technology and Uppsala University. C.L. and M.K. are supported by funds to Dept. of Civil Engineering, National Chung Hsing University (NCHU), from Ministry of Science and Technology, Taiwan (nos. MOST 105-2221-E-005-033-MY3, MOST 106-2221-E-005-045-MY3, and MOST 106-2911-I-006-301).

Acknowledgments: The research is a part of the collaboration starting from 2012 between National Chung Hsing University, Taiwan, and Royal Institute of Technology, Sweden. The authors are grateful to Prof. Nobuhito Mori of Kyoto University Disaster Prevention Research Institute for providing the air-bubble tracking software. We also give our thanks to other participants on the project, including Miss Wei-Ying Wong and Mr. Chia-Fon Fu at NCHU. The authors would like to express their sincere appreciation to UTOPIA Instruments Co., Ltd. for testing the high-speed digital camera and to the anonymous reviewers for their suggestions and comments that have led to improvements in the quality of the article.

Conflicts of Interest: The authors declare no conflict of interest.

References

1. Pfister, M.; Hager, W.H. Chute aerators (I): Air transport characteristics. *J. Hydraul. Eng.* **2010**, *136*, 352–359. [[CrossRef](#)]
2. Pfister, M.; Hager, W.H. Chute aerators (II): Hydraulic design. *J. Hydraul. Eng.* **2010**, *136*, 360–367. [[CrossRef](#)]
3. Pan, S.; Shao, Y.; Shi, Q.; Dong, X. The self-aeration capacity of the water jet over the aeration ramp. *J. Hydraul. Eng.* **1980**, *5*, 13–22. (In Chinese with English Abstract).
4. Pinto, N.L.; Neidert, S.H.; Ota, J.J. Aeration at high velocity flows. *Water Power Dam Constr.* **1982**, *34*, 42–44.
5. Pinto, N.L.; Neidert, S.H. Evaluating entrained air flow through aerators. *Water Power Dam Constr.* **1983**, *35*, 40–42.
6. Wood, I.R. Air entrainment in high speed flows. In Proceedings of the Symposium on Scale Effects in Modelling Hydraulic Structures, Esslingen am Neckar, Germany, 3–6 September 1984; Kobus, H., Ed.; Technische Akademie Esslingen: Esslingen am Neckar, Germany, 1984.
7. Volkart, P.; Rutschmann, P. Rapid flow in spillway chutes with and without deflectors—A model-prototype comparison. In Proceedings of the Symposium on Scale Effects in Modelling Hydraulic Structures, Esslingen am Neckar, Germany, 3–6 September 1984; Kobus, H., Ed.; Technische Akademie Esslingen: Esslingen am Neckar, Germany, 1984.
8. Marcano, A.; Castillejo, H. Model-prototype comparison of aeration devices of Guri Spillway. In Proceedings of the Symposium on Scale Effects in Modelling Hydraulic Structures, Esslingen am Neckar, Germany, 3–6 September 1984; Kobus, H., Ed.; Technische Akademie Esslingen: Esslingen am Neckar, Germany, 1984.
9. Pan, S.; Shao, Y. Scale effects in modeling air demand by a ramp slot. In Proceedings of the Symposium on Scale Effects in Modelling Hydraulic Structures, Esslingen am Neckar, Germany, 3–6 September 1984; Kobus, H., Ed.; Technische Akademie Esslingen: Esslingen am Neckar, Germany, 1984.
10. Falvey, H.T.; Irvine, D.A. Aeration in jets and high speed flows. In Proceedings of the International Symposium on Model-Prototype Correlation of Hydraulic Structures, Colorado Springs, CO, USA, 9–11 August 1988; Burgi, P.H., Ed.; American Society of Civil Engineers (ASCE): New York, NY, USA, 1988.
11. Rutschmann, P. Calculation and optimum shape of spillway chute aerators. In Proceedings of the International Symposium on Model-Prototype Correlation of Hydraulic Structures, Colorado Springs, CO, USA, 9–11 August 1988; Burgi, P.H., Ed.; American Society of Civil Engineers (ASCE): New York, NY, USA, 1988.
12. Wood, I.R. Aerators—The interaction of nappe and duct air entrainment. In *Proceedings of the International Symposium on Hydraulics for High Dams*; IAHR: Beijing, China, 1998; pp. 611–618.
13. Rutschmann, P.; Hager, W.H. Air entrainment by spillway aerators. *J. Hydraul. Eng.* **1990**, *116*, 765–782. [[CrossRef](#)]
14. Gaskin, S.; Aubel, T.; Holder, G. Air demand for a ramp-offset aerator as a function of spillway slope, ramp angle and Froude number. In Proceedings of the 30th IAHR Congress, Thessaloniki, Greece, 24–29 August 2003; Ganoulis, J.J., Prinos, P., Eds.; International Association of Hydraulic Engineering and Research (IAHR): Delft, The Netherlands, 2003.
15. Kramer, K.; Hager, W.H.; Minor, H.E. New model investigations on two-phase chute flow. In *Hydraulics of Dams and River Structures*; CRC Press: London, UK, 2004; pp. 33–41.
16. Kramer, K.; Hager, W.H. Air transport in chute flows. *Int. J. Multiph. Flow* **2005**, *31*, 1181–1197. [[CrossRef](#)]
17. Kramer, K.; Hager, W.H.; Minor, H.E. Development of air concentration on chute spillways. *J. Hydraul. Eng.* **2006**, *132*, 908–915. [[CrossRef](#)]

18. Jalili Ghazizadeh, M.R.; Esfandiari, S.; Ahmadi, A.; Zarrati, A.R. Hybrid model approach and combination of physical approaches with numerical simulation. In Proceedings of the IAHR Congress, Nanjing, China, 13–15 September 2010; Nanjing Hydraulic Research Institute: Nanjing, China, 2010.
19. Pfister, M. Chute aerator: Steep deflectors and cavity sub-pressure. *J. Hydraul. Eng.* **2011**, *137*, 1208–1215. [[CrossRef](#)]
20. Resch, F.J.; Leutheusser, H.J.; Alemu, S. Bubbly two-phase flow in hydraulic jump. *J. Hydraul. Div.* **1974**, *100*, 137–149.
21. Mossa, M.; Tolve, U. Flow visualization in bubbly two-phase hydraulic jump. *J. Fluid Eng.* **1998**, *120*, 160–165. [[CrossRef](#)]
22. Chanson, H.; Brattberg, T. Experimental study of the air-water shear flow in a hydraulic jump. *Int. J. Multiph. Flow* **2000**, *26*, 583–607. [[CrossRef](#)]
23. Murzyn, F.; Mouaze, D.; Chaplin, J.R. Optical fiber probe measurements of bubbly flow in hydraulic jump. *Int. J. Multiph. Flow* **2005**, *31*, 141–154. [[CrossRef](#)]
24. Hornung, H.G.; Willert, C.; Turner, S. The flow field downstream of a hydraulic jump. *J. Fluid Mech.* **1995**, *287*, 299–316. [[CrossRef](#)]
25. Lennon, J.M.; Hill, F.D. Particle image velocity measurements of undular and hydraulic jumps. *J. Hydraul. Eng.* **2006**, *132*, 1283–1294. [[CrossRef](#)]
26. Misra, S.K.; Kirby, J.T.; Brocchini, M.; Veron, F.; Thomas, M.; Kambhamettu, C. The mean and turbulent flow structure of a weak hydraulic jump. *Phys. Fluids* **2008**, *20*. [[CrossRef](#)]
27. Bercovitz, Y.; Lebert, F.; Jodeau, M.; Buvat, C.; Violeau, D.; Pelaprat, L.; Hajczak, A. LS-PIV procedure applied to a plunging water jet issuing from an overflow nappe. In Proceedings of the 4th IAHR Europe Congress of Sustainable Hydraulics in the Era of Global Change, Liege, Belgium, 27–29 July 2016; Erpicum, S., Dewals, B., Archambeau, P., Piroton, M., Eds.; Taylor & Francis Group: London, UK, 2016. ISBN 978-1-138-02977-4.
28. Chang, K.A.; Lim, H.J.; Su, C.B. Fiber optic reflectometer for velocity and void fraction measurements in multiphase flows. *Rev. Sci. Instrum.* **2003**, *74*, 3559–3565. [[CrossRef](#)]
29. Ryu, Y.; Chang, K.A.; Lim, H.J. Use of bubble image velocimetry for measurement of plunging wave impinging on structure and associated greenwater. *Meas. Sci. Technol.* **2005**, *16*, 1945–1953. [[CrossRef](#)]
30. Ryu, Y.; Chang, K.A.; Mercier, R. Runup and green water velocities due to breaking wave impinging and overtopping. *Exp. Fluids* **2007**, *43*, 555–567. [[CrossRef](#)]
31. Kashima, H.; Mori, N.; Kakuno, S. Air-bubble measurements of the surf zone breaking waves by bubble tracking velocimetry. In *Proceedings of International Conference on Coastal Engineering*; ASCE: San Diego, CA, USA, 2006; pp. 934–945.
32. Mori, N.; Suzuki, T.; Kakuno, S. Experimental study of air bubbles and turbulence characteristics in the surf zone. *J. Geophys. Res.* **2007**, *112*. [[CrossRef](#)]
33. Mori, N.; Kakuno, S. Aeration and bubble measurements of coastal breaking waves. *Fluid Dyn. Res.* **2008**, *40*, 616–626. [[CrossRef](#)]
34. Lin, C.; Hsieh, S.C.; Kuo, M.J.; Chang, K.A. Periodic oscillation caused by a uniform flow over a vertical drop energy dissipater. *J. Hydraul. Eng.* **2008**, *134*, 948–960. [[CrossRef](#)]
35. Lin, C.; Hsieh, S.C.; Lin, Y.R.; Chang, K.A.; Raikar, R.V. Flow property and self-similarity in steady hydraulic jumps. *Exp. Fluids* **2012**, *53*, 1591–1616. [[CrossRef](#)]
36. Karn, A.; Ellis, C.; Arndt, R.; Hong, J. An integrative image measurement technique for dense bubbly flow with a wide size distribution. *Chem. Eng. Sci.* **2015**, *122*, 240–249. [[CrossRef](#)]
37. Besagni, G.; Inzoli, F. Bubble size distributions and shapes in annular gap bubble column. *Exp. Therm. Fluid Sci.* **2016**, *74*, 27–48. [[CrossRef](#)]
38. Lin, C.; Kao, M.J.; Yang, J.; Teng, P.H.; Raikar, R.V. Study on probabilistic mean features of lower and upper free-surface profiles and velocity fields of a highly fluctuating free jet over a chute. *J. Mar. Sci. Technol.* **2018**, *26*, 309–326.
39. Gonzalez, R.C.; Woods, R.E. *Digital Image Processing*, 3rd ed.; Prentice Hall: Upper Saddle River, NJ, USA, 2008; pp. 104–143. ISBN 978-0131687288.
40. Gonzalez, R.C.; Woods, R.E.; Eddins, S.L. *Digital Image Processing Using Matlab*, 2nd ed.; Gatesmark Publishing: Knoxville, TN, USA, 2009; ISBN 978-0-9820854-0-0.
41. Li, Y.D. Investigation on the Two-Phase Flow Field of a Chute Flow with Bottom Aerator. Master's Thesis, National Chung Hsing University, Taichung, Taiwan, 2014.

42. Mori, N.; Chang, K.A. *Introduction to MPIV—PIV Toolbox in Matlab*. User Reference Manual. 2009, pp. 1–15. Available online: <http://www.oceanwave.jp/software/mpiv/index.php?Download> (accessed on 1 November 2018).
43. Adrian, R.J. Particle imaging techniques for experimental fluid mechanics. *Annu. Rev. Fluid Mech.* **1991**, *23*, 261–304. [[CrossRef](#)]
44. Keane, R.D.; Adrian, R.J. Theory of cross-correlation analysis of PIV images. *Appl. Sci. Res.* **1992**, *49*, 191–215. [[CrossRef](#)]
45. Lin, C.; Huang, W.Y.; Hsieh, S.C.; Chang, K.A. Experimental study on mean velocity characteristics of flow over vertical drop. *J. Hydraul. Res.* **2007**, *45*, 33–42. [[CrossRef](#)]
46. Lin, C.; Hsieh, W.Y.; Hsieh, S.C.; Chang, K.A. Reply to the Discussion of: Experimental study on mean velocity characteristics of flow over vertical drop. *J. Hydraul. Res.* **2008**, *46*, 424–428.
47. Lin, C.; Lin, W.J.; Hsieh, S.C.; Chou, S.H.; Raikar, R.V. Velocity and turbulence characteristics of skimming flow over a vertical drop without end sill. *J. Mech.* **2012**, *28*, 607–626. [[CrossRef](#)]
48. Shi, Q.S. *High-Velocity Aerated Flow*; China Water and Power Press: Beijing, China, 2007; pp. 273–296. ISBN 978-7-5084-5055-1.
49. Bendat, J.S.; Piersol, A.G. *Random Data Analysis and Measurement Procedures*, 2nd ed.; John Wiley & Sons: Singapore, 1991; pp. 109–120. ISBN 9971-51-071-5.
50. Tennekes, H.; Lumley, J.L. *A First Course in Turbulence*, 1st ed.; MIT Press: Cambridge, UK, 1987; pp. 210–212. ISBN 9780262200196.
51. Rajaratnam, N.; Chamani, M.R. Energy loss at drops. *J. Hydraul. Res.* **1995**, *33*, 373–384. [[CrossRef](#)]
52. Zhou, Y.L.; Li, H.C.; Sun, B. *Multiphase Flow Parameters Measurement Based on Digital Image Processing Technology*; Science Publication, Inc.: Beijing, China, 2012; pp. 15–38. ISBN 978-7-03-033650-7.
53. Sonka, M.; Hlavac, H.; Boyle, R. *Image Processing, Analysis, and Machine Vision*, 3rd ed.; Cengage Learning Publishing: Mason, OH, USA, 2007; pp. 507–542. ISBN 9780495244387.
54. Catt, F.; Lions, P.L.; Morel, J.M. Image selective smoothing and edge detection by nonlinear diffusion. *SIAM J. Numer. Anal.* **1992**, *29*, 182–193. [[CrossRef](#)]
55. Chen, T.F.; Vese, L.A. Active contours without edges. *IEEE Trans. Image Process.* **2001**, *10*, 266–277. [[CrossRef](#)] [[PubMed](#)]
56. Lindken, R.; Merzkirch, W. A novel PIV technique for measurements in multiphase flows and its application to two-phase bubbly flows. *Exp. Fluids* **2002**, *33*, 814–825. [[CrossRef](#)]
57. Shi, L.L.; Cai, J.H.; Zhou, Z.K. Gas-Liquid two phase flow pattern identification based on image processing. *J. Zhejiang Univ.* **2005**, *39*, 1128–1131.
58. Adrian, R.J.; Westerweel, J. *Particle Image Velocimetry*; Cambridge University Press: New York, NY, USA, 2011; pp. 241–267. ISBN 978-0-521-44008-0.
59. Lee, S.J.; Kawakami, K.; Arndt, R.E.A. Application of a shadow image velocimetry to a ventilated hydrofoil wake. *J. Vis.* **2014**, *17*, 327–335. [[CrossRef](#)]

